Causes of Climate Variability

- **Natural origin**

  external: land-sea distribution, orography

  solar constant, orbital variations

  volcano

  internal variability of the climate system

  (e.g., air-sea interaction,,,)

- **Anthropogenic origin**

  emission of greenhouse gases, destruction of ozone layer, land surface modification,,,

Extratropical Disturbances

Monthly Weather Review, 1992

Rossby-wave Propagation

Global Teleconnections in the 250-mb Streamfunction Field during the Northern Hemisphere Winter

HUANG-HSIUNG HSU AND SHIH-HSUN LIN

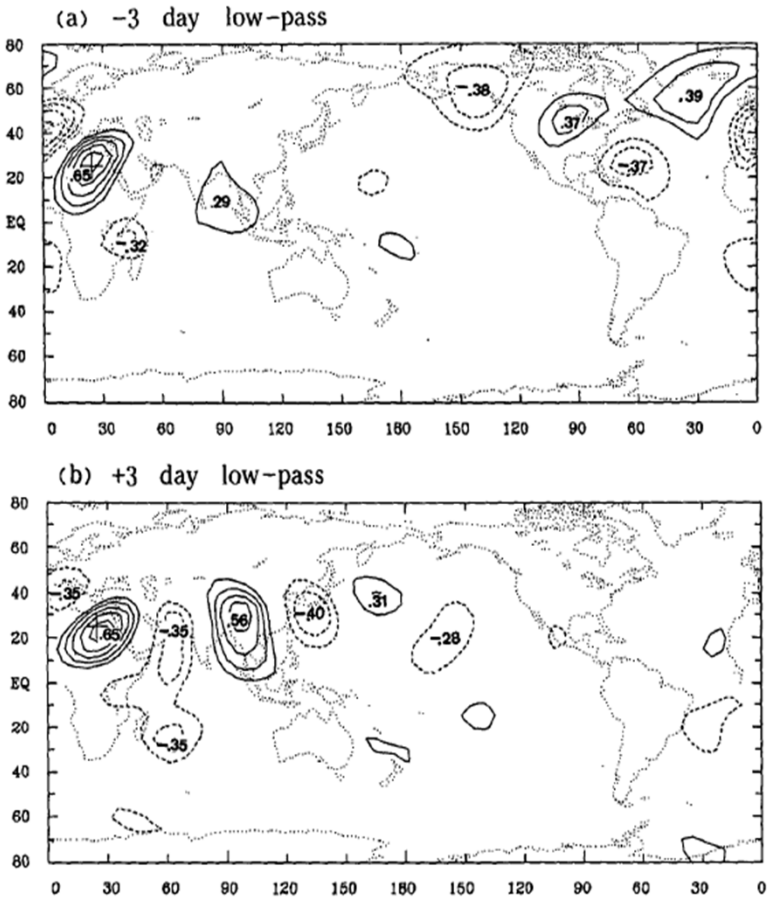

FIG. 7. Same as in Figs. 5a,b but for base point (25°N, 25°E).

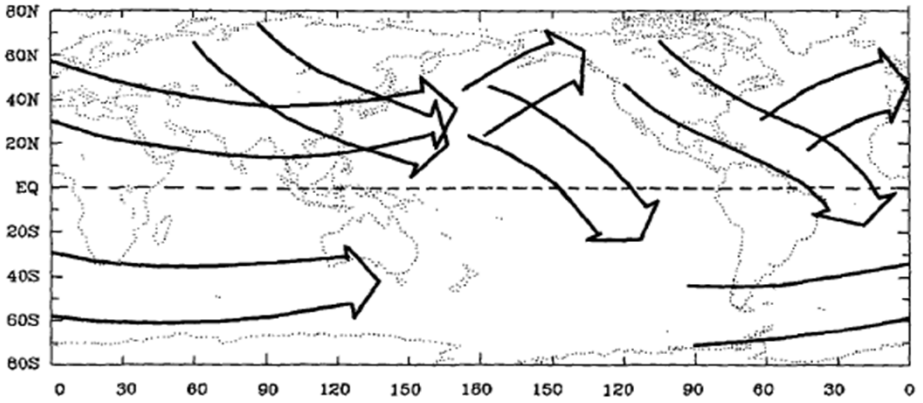

FIG. 14. Schematic plot of seven waveguides deduced from lag-correlation maps for the base points in the vicinity of maximum teleconnectivity.

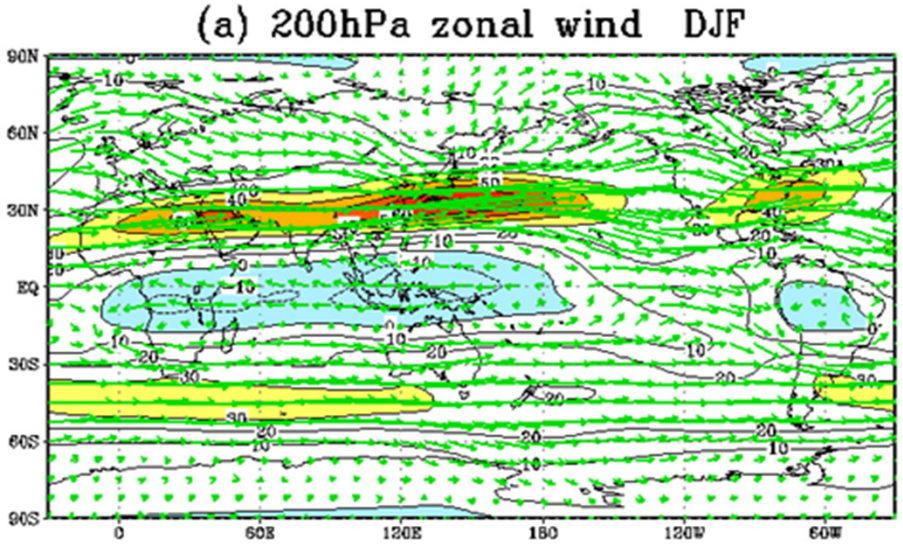

Tropical Disturbances

In Tropics, Heavy Precipitation -> Deep Cloud -> OLR

- Outgoing Longwave Radiation (OLR) from

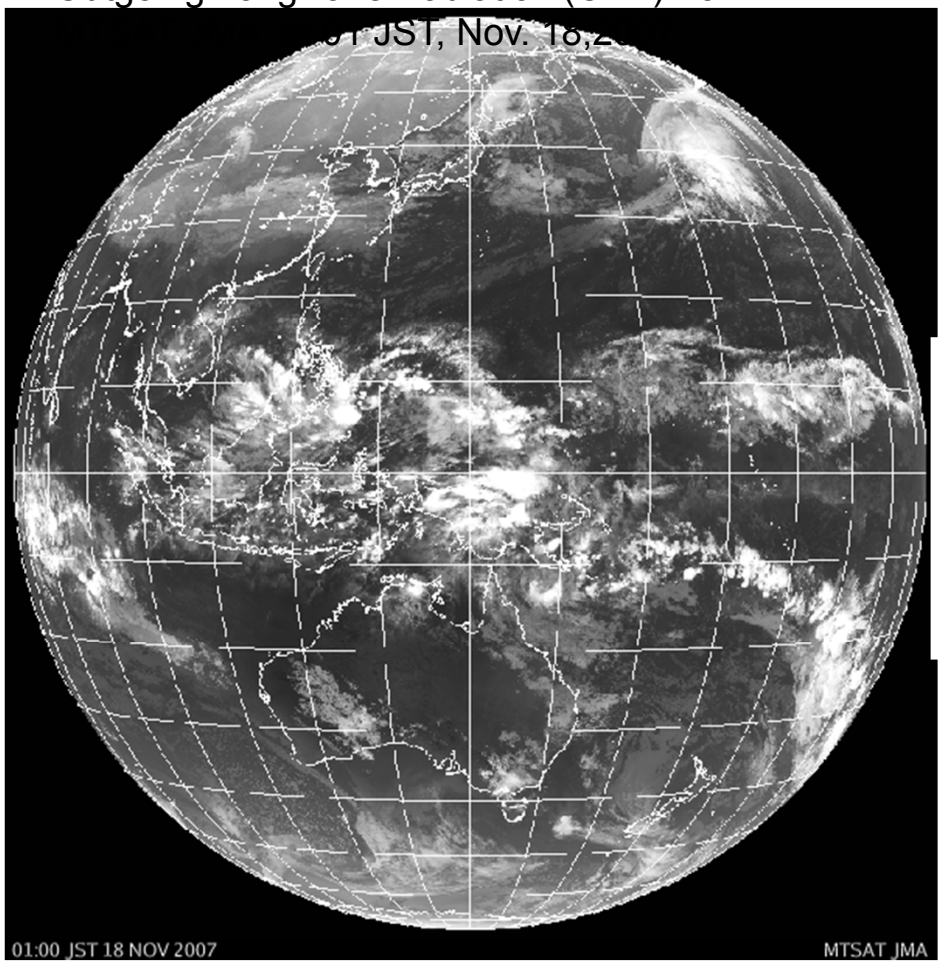

OLR variance in all planetary to synoptic scales

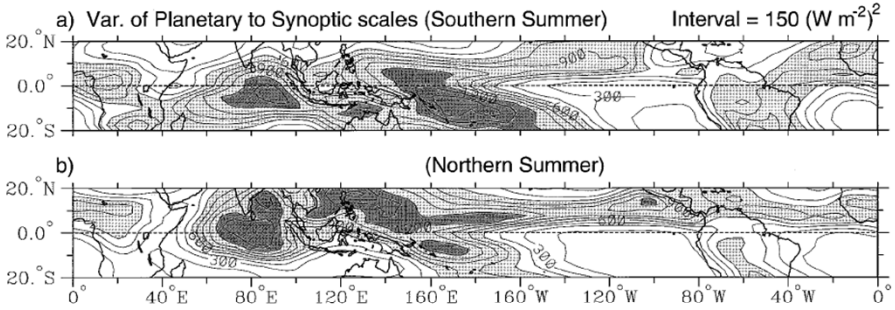

From Wheeler, M., and G. N. Kiladis, 1999

Wheeler, M., and G. N. Kiladis, 1999: Convectively coupled equatorial waves: Analysis of clouds in the wavenumber frequency domain. *J. Atmos. Sci.*, **56,** 374–399.

Red Noise

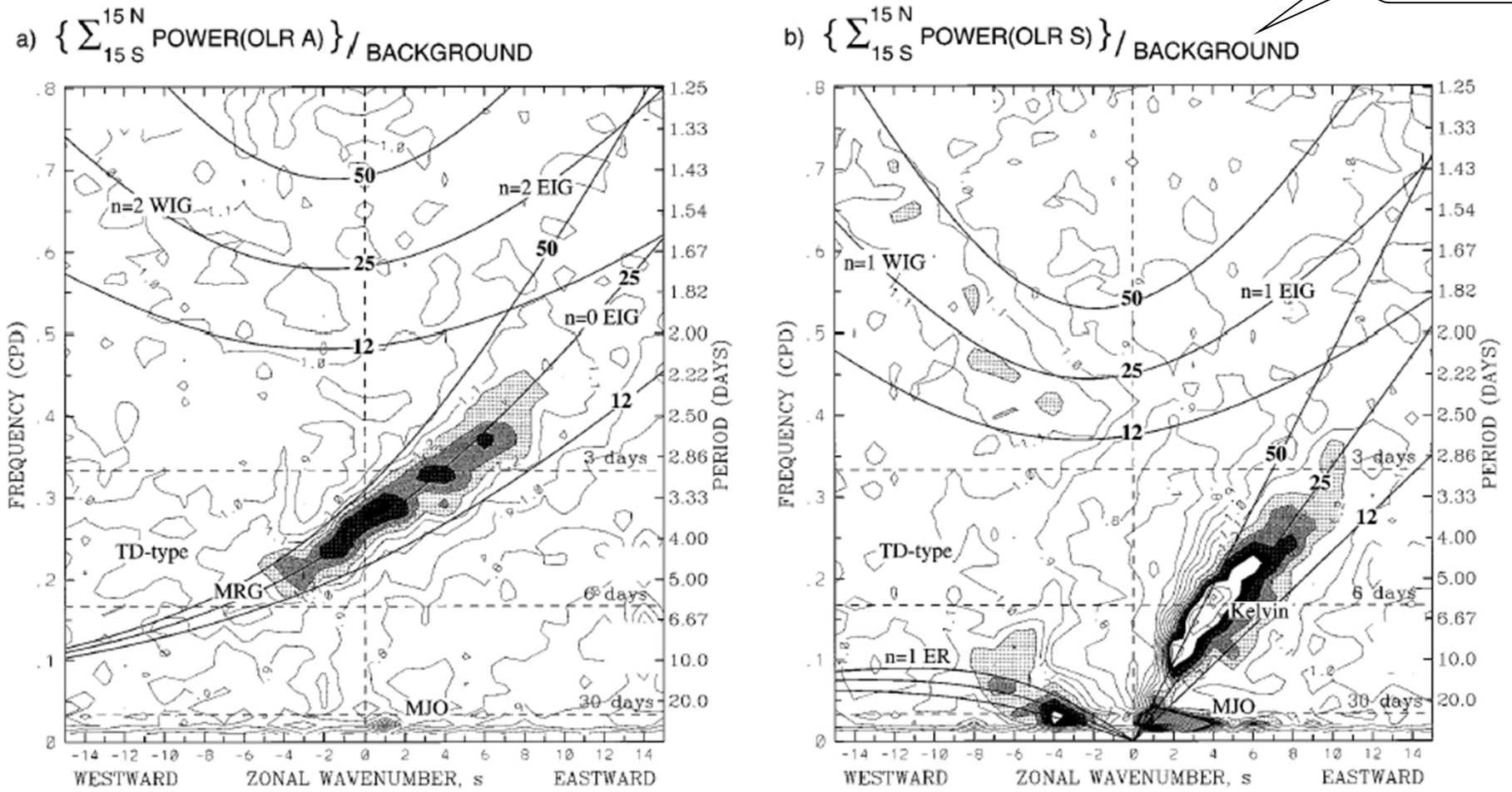

FIG. 3. (a) The antisymmetric OLR power of Fig. 1a divided by the background power of Fig. 2. Contour interval is 0.1, and shading begins at a value of 1.1 for which the spectral signatures are statistically significantly above the background at the 95% level (based on 500 dof). Superimposed are the dispersion curves of the even meridional mode-numbered equatorial waves for the three equivalent depths of h = 12, 25, and 50 m. (b) Same as in panel a except for the symmetric component of OLR of Fig. 1b and the corresponding odd meridional mode-numbered equatorial waves. Frequency spectral bandwidth is 1/96 cpd.

Easterly waves and Tropical Depression (TD) -type disturbances

TD best tracks

from Jun Yoshimura at MRI/JMA

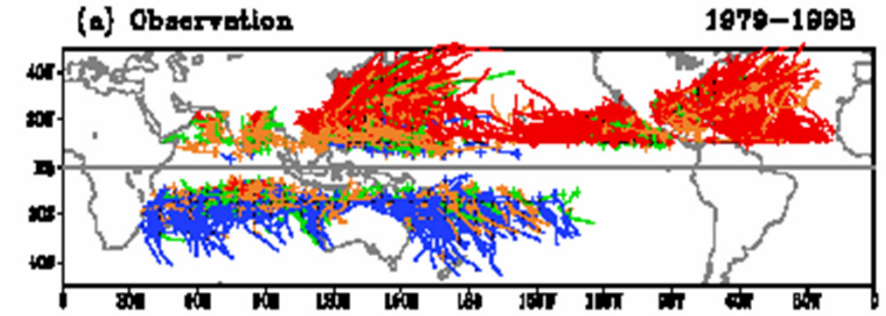

Roundy, P. and William M. Frank, 2004: A Climatology of Waves in the Equatorial Region. *J.Atmos.Sci.,* **61**, 2105-2132.

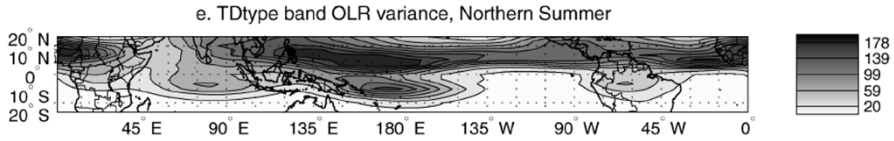

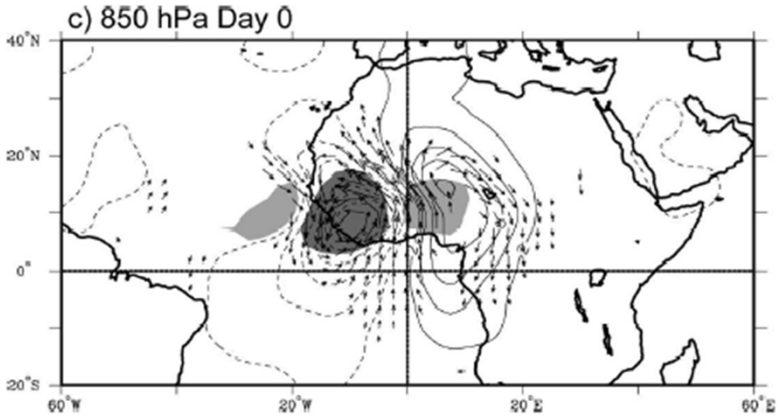

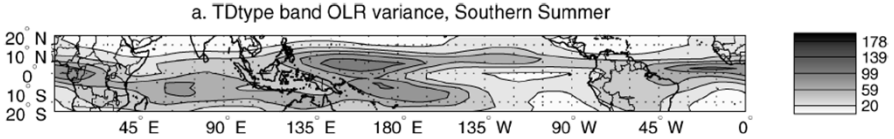

Kiladis, G.N., C. D.Thorncroft, and N. M. J. Hall,2006: Three-Dimensional Structure and Dynamics of African Easterly Waves. Part I: Observations. *J. Atmos. Sci.,* **63**, 2212-2230.

Wheeler, M., and G. N. Kiladis, 1999

Decomposition of OLR anomalies

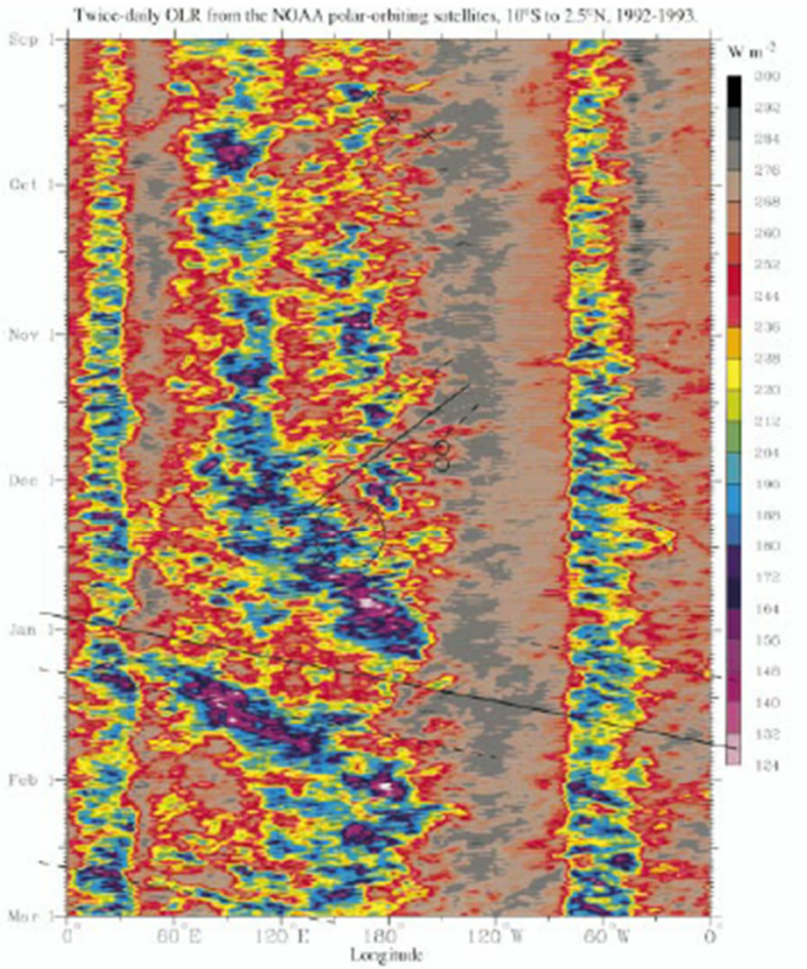

FIG. 8. Time-longitude section of the twice-daily total OLR (W m^{-2}) averaged for the latitudes from 10°S to 2.5°N and for 6 Z 1 September 1992 through 6 Z 1 March 1993. Values correspond to the color bar. Each time section consists of half nighttime and half daytime data from the polar-orbiting satellite (see text for details). Dark lines, circles, and crosses refer to convectively coupled equatorial wave disturbances, and match those of Fig. 9.

FIG. 9. (a) Time-longitude section of the OLR anomalies for the MJO-filtered band for the same 6-month sample period as Fig. 8, averaged for the latitudes from 10°S to 2.5°N. The zero contour has been omitted. Light shading for positive anomalies and dark shading and dashed contours for negative anomalies. (b) Same as in panel a except for the Kelvin wave–filtered band. (c) The $n = 1$ ER wave–filtered band. (d) The MRG wave–filtered band.

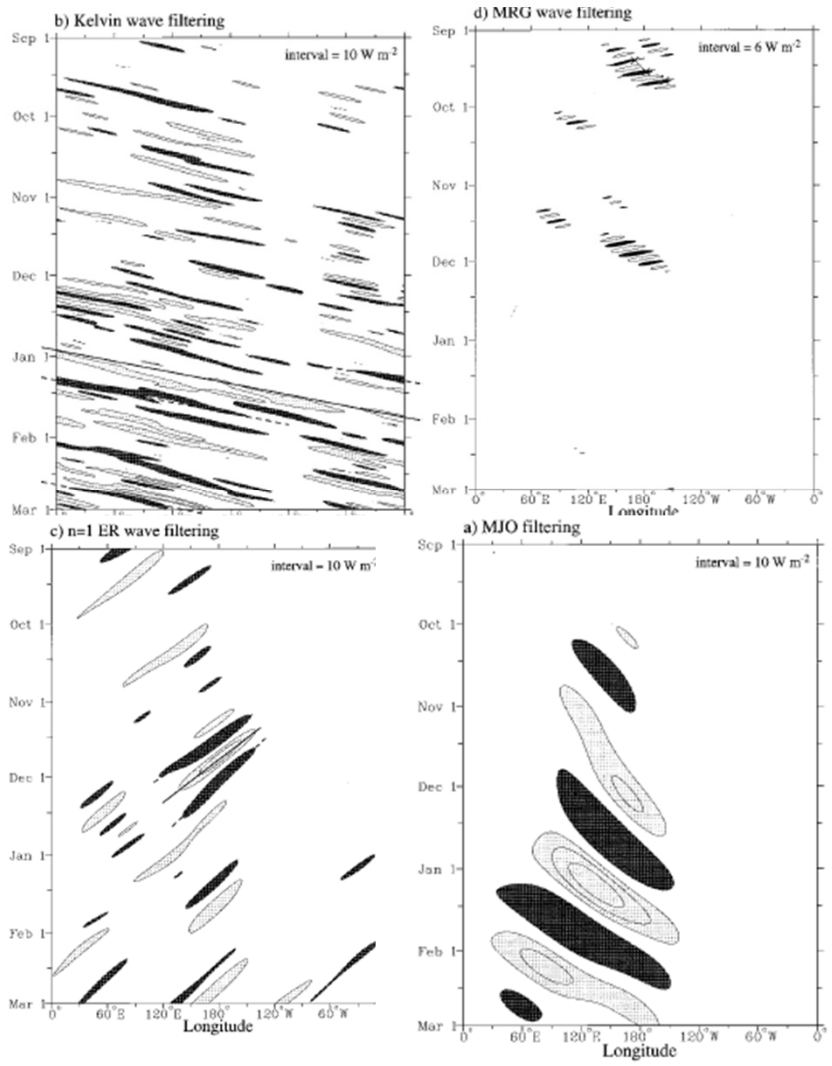

From Madden and Julian (1972)

Madden-Julian Oscillation (MJO)

Surface pressure at Canton Iceland (3S, 172W)

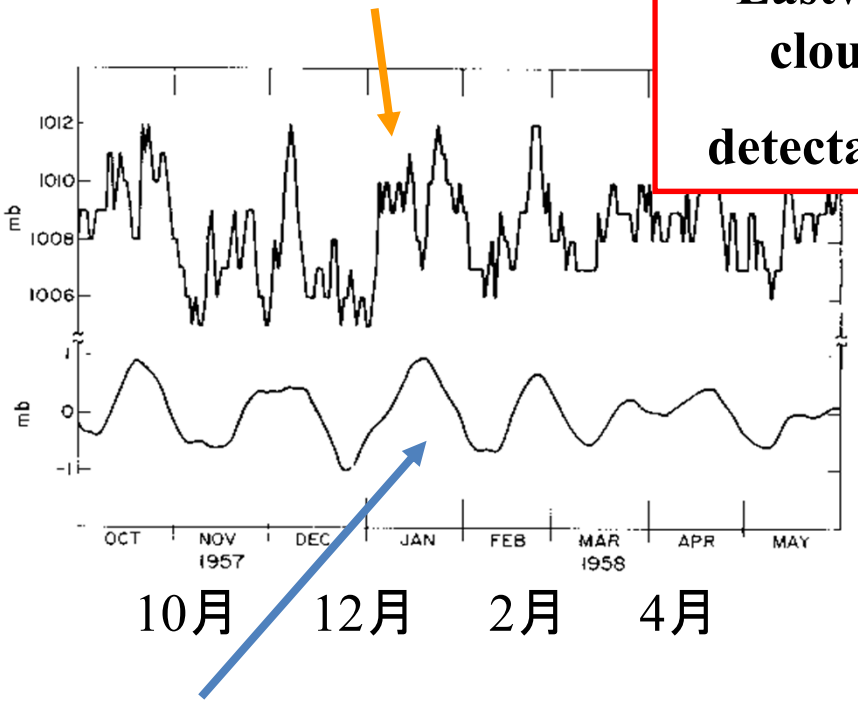

After applying band-pass filter around 45 days

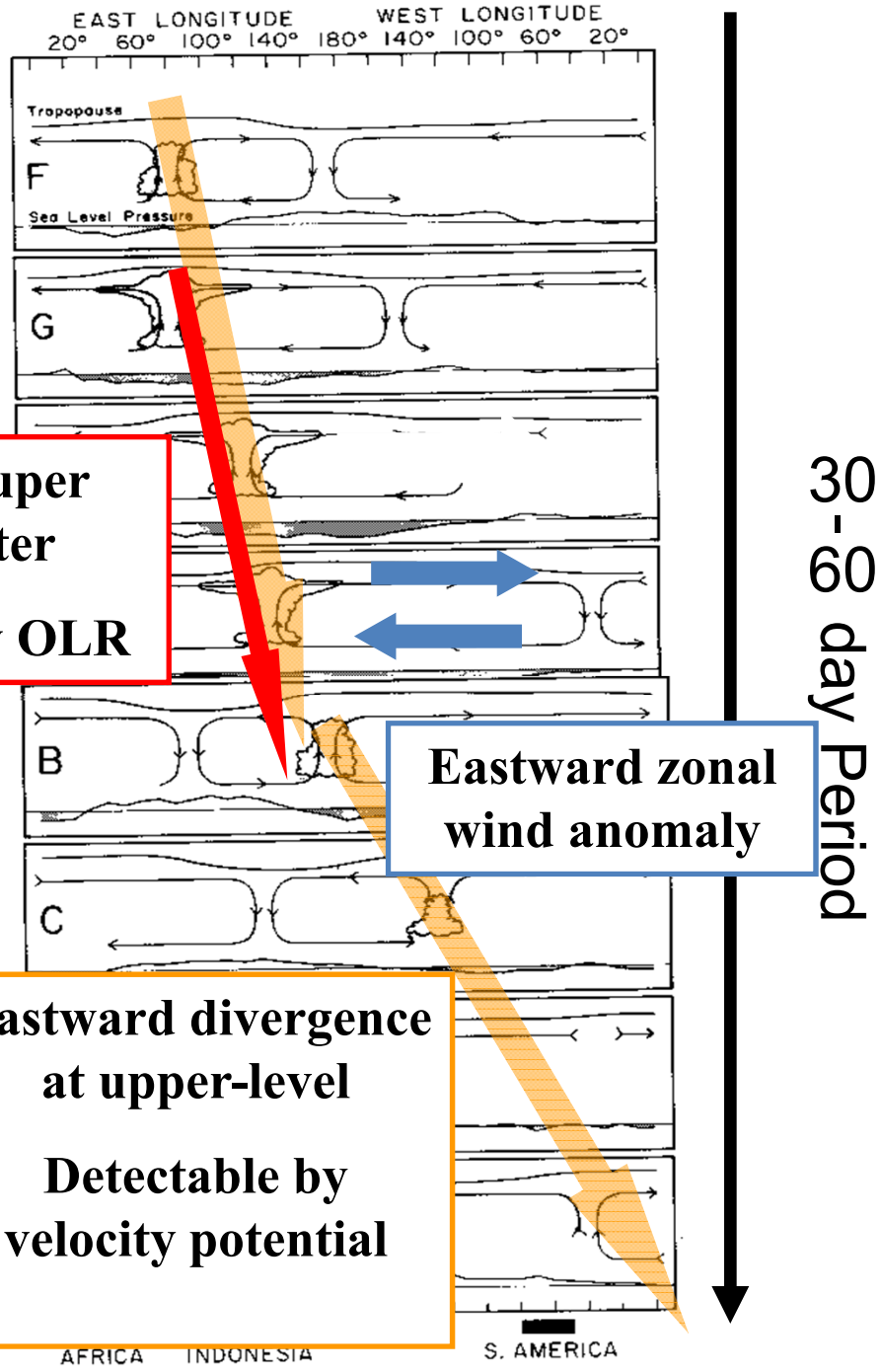

Eastward super cloud cluster

detectable by OLR

Eastward zonal wind anomaly

Eastward divergence at upper-level

Detectable by velocity potential

30-60 day Period

From Knutson and Weickmann (1987)

250 hPa streamfunction and OLR composites at phases of MJO

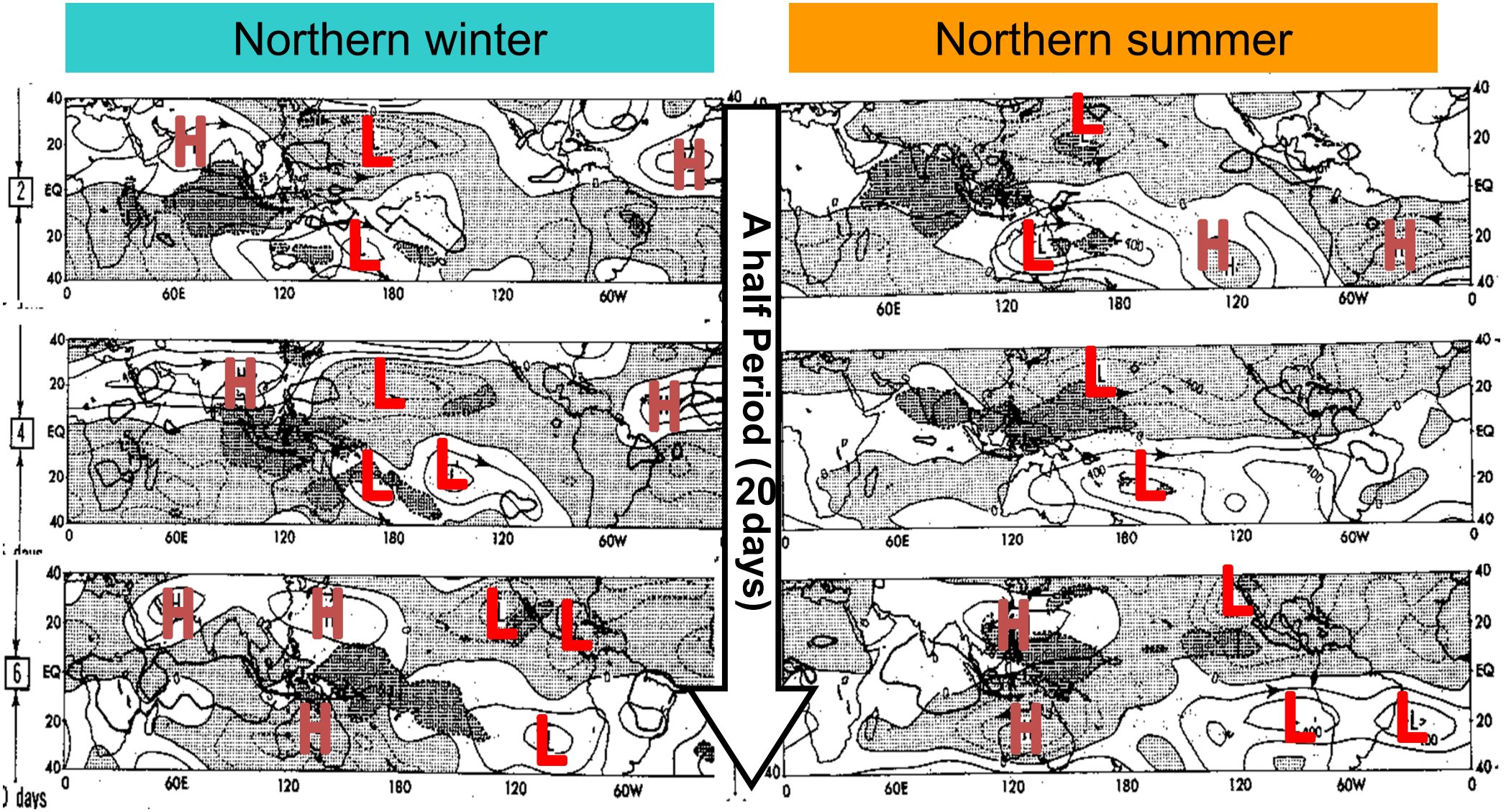

Wheeler, M., and G. N. Kiladis, 1999

Decomposition of OLR anomalies

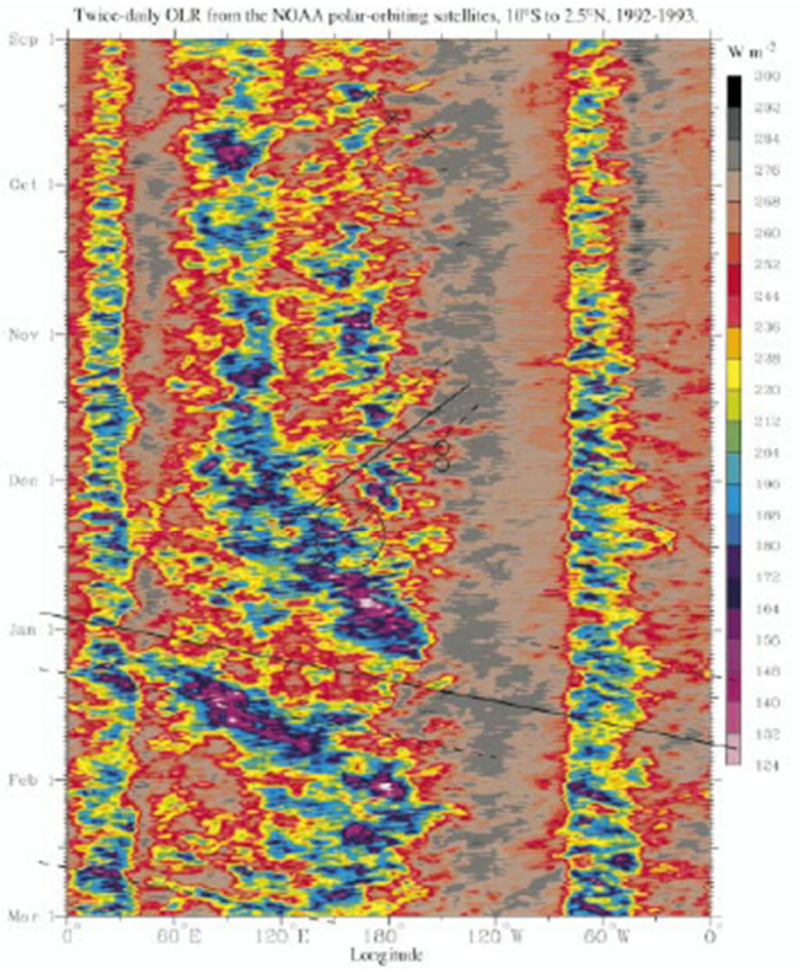

FIG. 8. Time-longitude section of the twice-daily total OLR (W m^{-2}) averaged for the latitudes from 10°S to 2.5°N and for 6 Z 1 September 1992 through 6 Z 1 March 1993. Values correspond to the color bar. Each time section consists of half nighttime and half daytime data from the polar-orbiting satellite (see text for details). Dark lines, circles, and crosses refer to convectively coupled equatorial wave disturbances, and match those of Fig. 9.

FIG. 9. (a) Time-longitude section of the OLR anomalies for the MJO-filtered band for the same 6-month sample period as Fig. 8, averaged for the latitudes from 10°S to 2.5°N. The zero contour has been omitted. Light shading for positive anomalies and dark shading and dashed contours for negative anomalies. (b) Same as in panel a except for the Kelvin wave–filtered band. (c) The $n = 1$ ER wave–filtered band. (d) The MRG wave–filtered band.

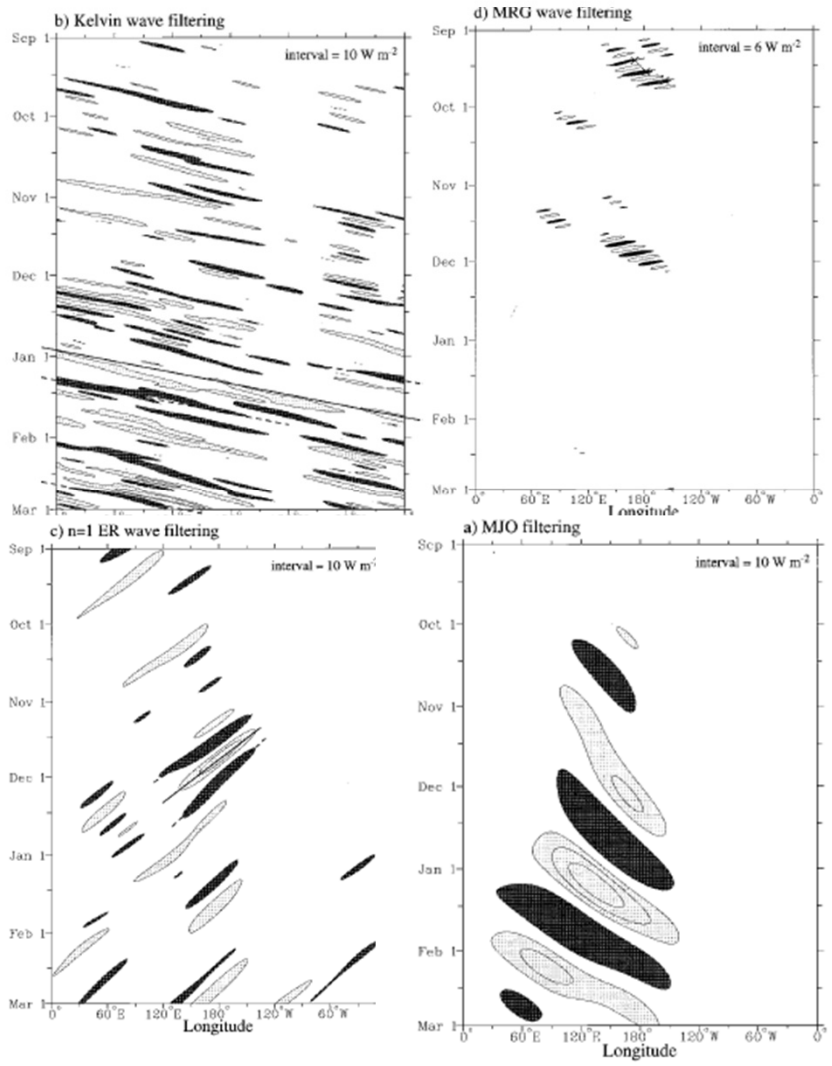

Matsuno, T., 1966: Quasi-geostrophic motions in the equatorial area. *J. Meteor. Soc. Japan,* **44,** 25–43.

Equatorial Waves

Kelvin wave

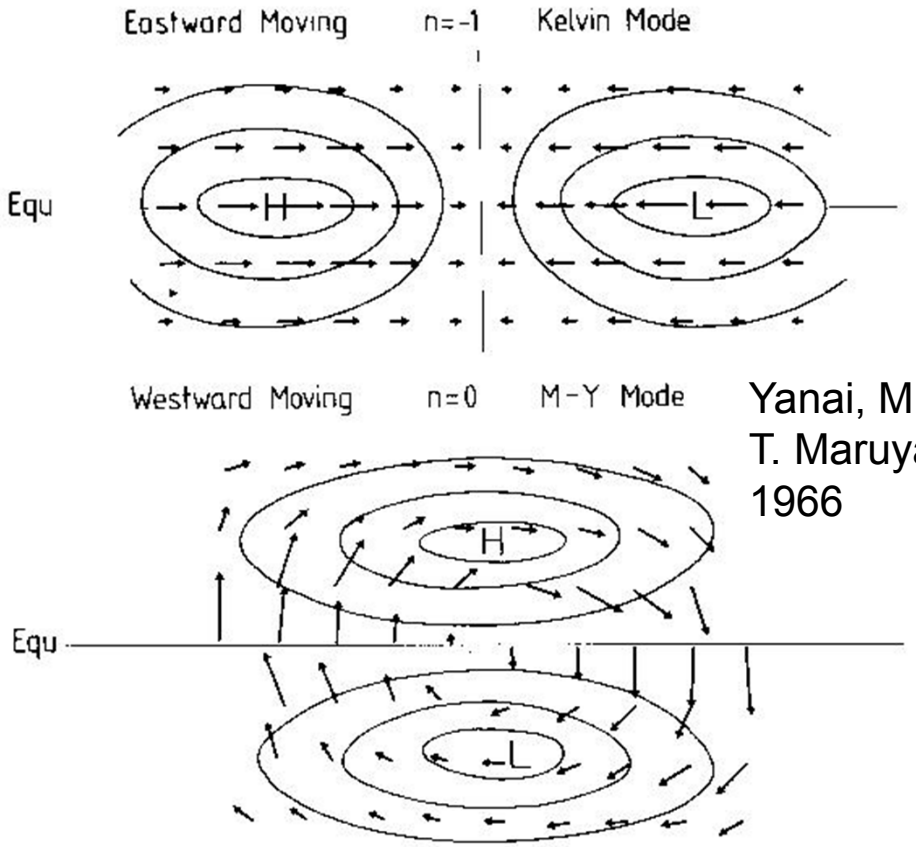

Yanai, M. and T. Maruyama, 1966

ER: Rossby wave (n=1)

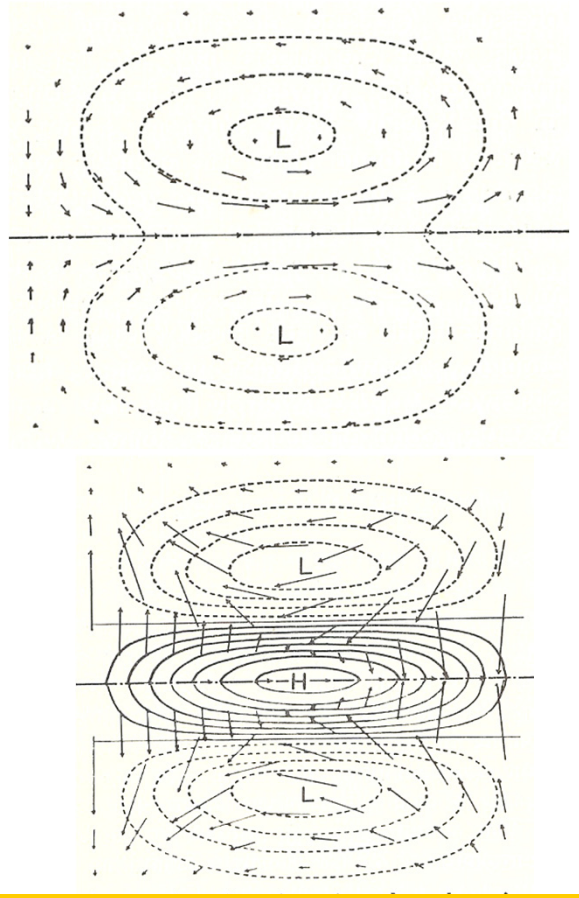

MRG : mixed Rossy-Gravity wave

EIG: eastward propagating inertio-gravity wave (n=1)

If a water mountain is put at the equator

How does it evolve next? => East-west asymmetry moving

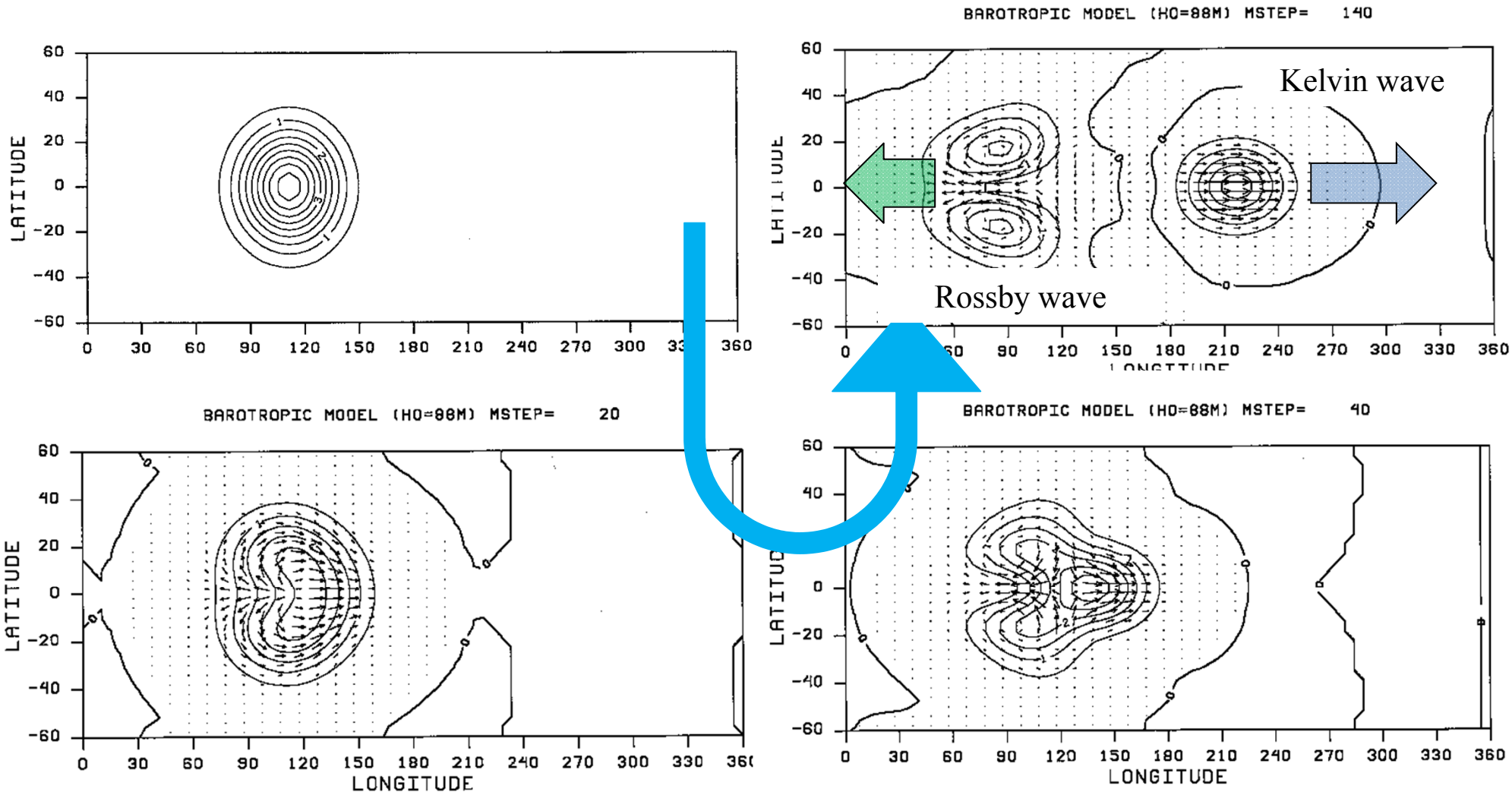

Some simple solutions for heat-induced tropical circulation

Quarterly Journal of the Royal Meteorological Society
Volume 106, Issue 449, July 1980, Pages: 447–462, A. E. Gill

Symmetric Heating Anomaly about the equator

Lower-layer wind (arrows) and vertical velocity (contours)

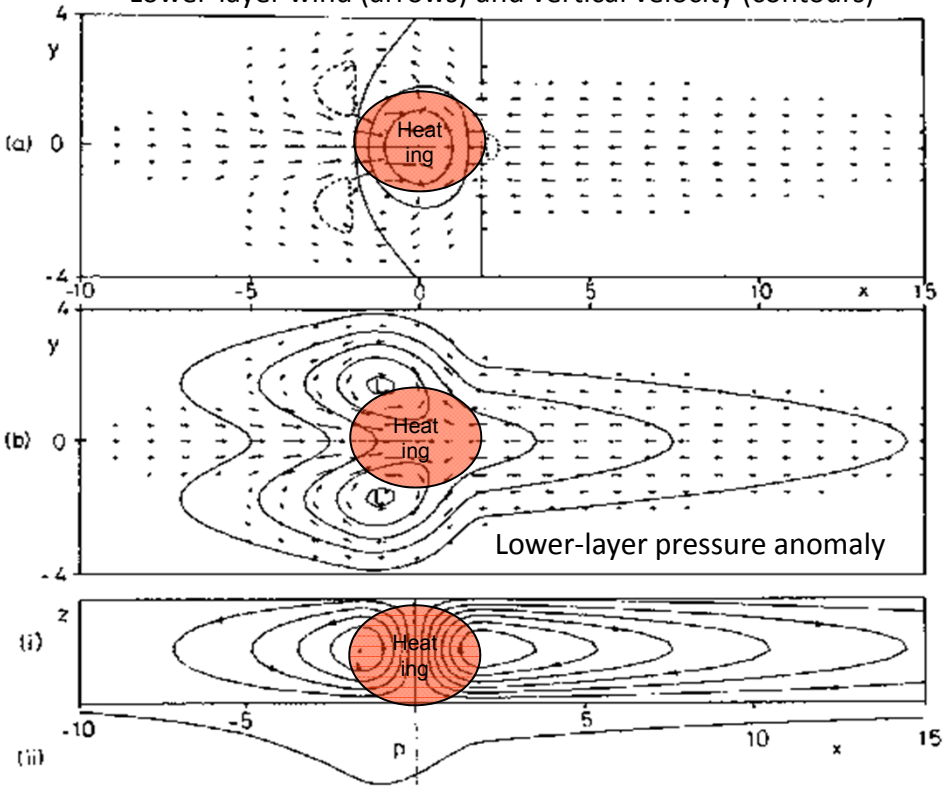

Asymmetric Heating Anomaly added about the equator

Lower-layer wind (arrows) and vertical velocity (contours)

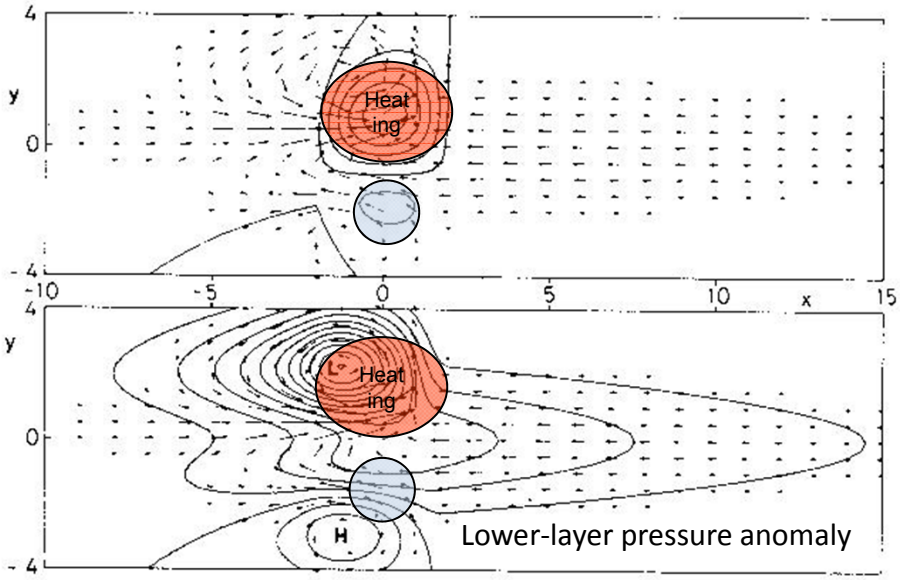

Vertical-longitudinal circulation

Seasonal to Interannual Variability

G1: ENSO and IOD : Seasonal Predictions

from JMA website

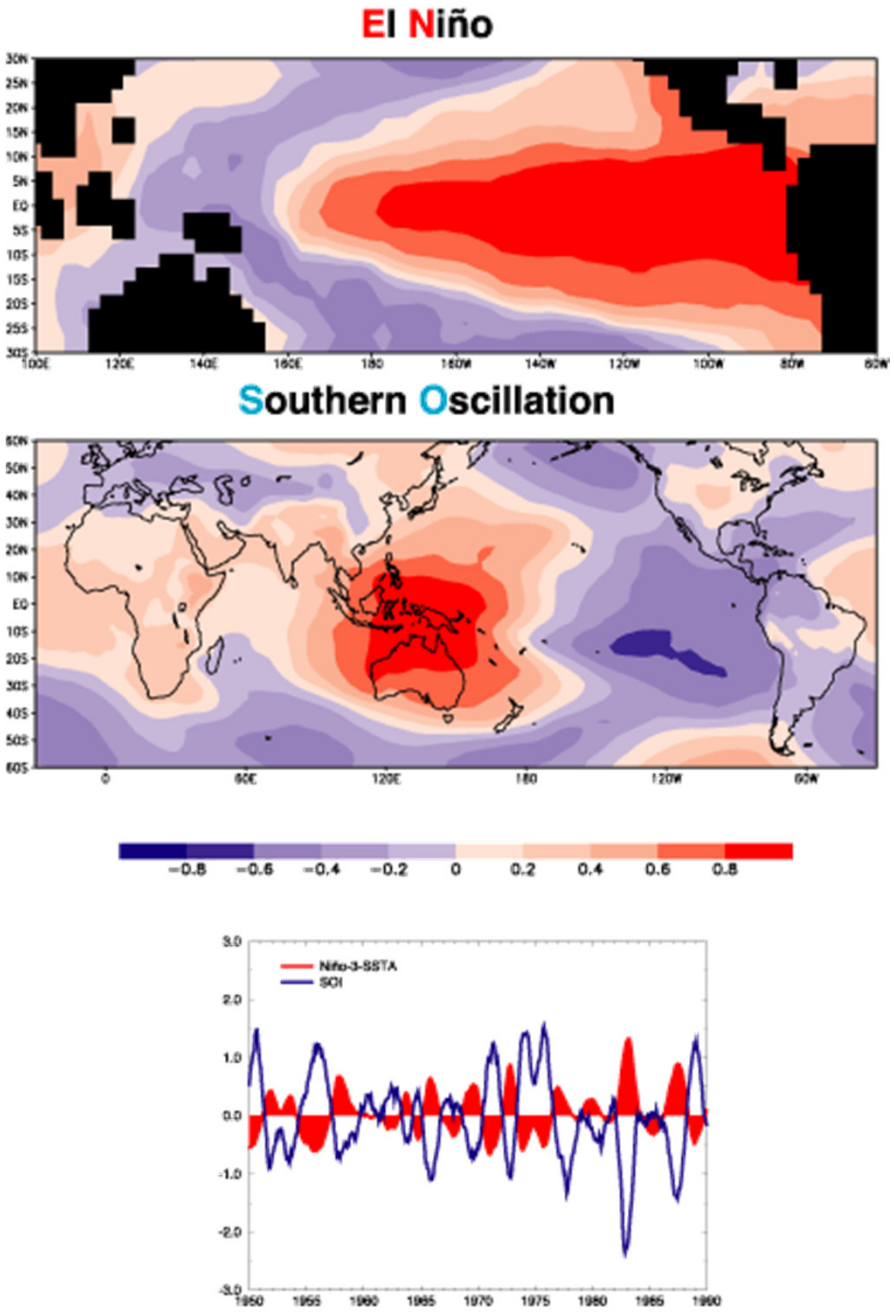

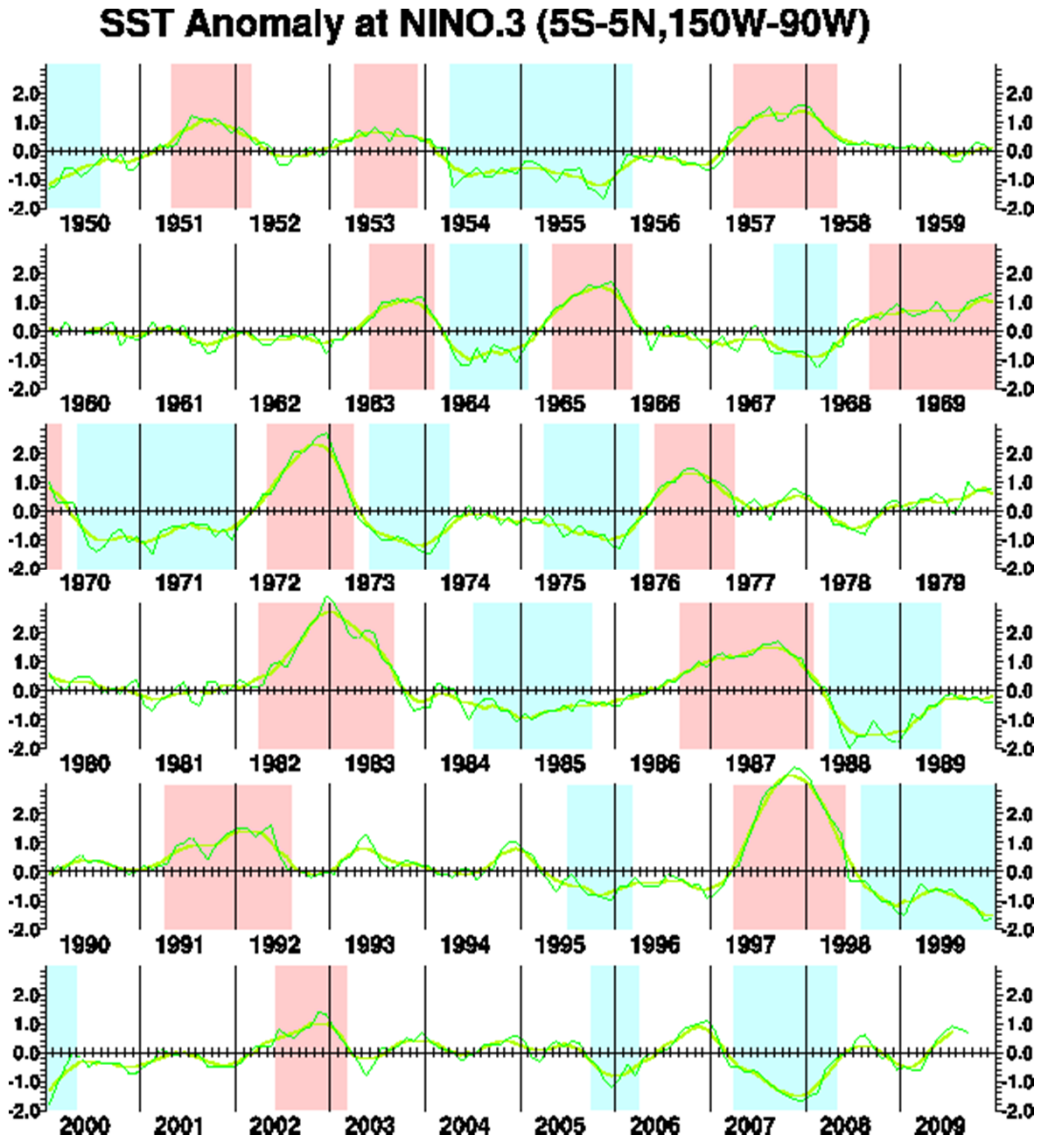

http://www.jamstec.go.jp/jamstec/TRITON/real_time/php/top.php

http://www.pmel.noaa.gov/tao/index.shtml

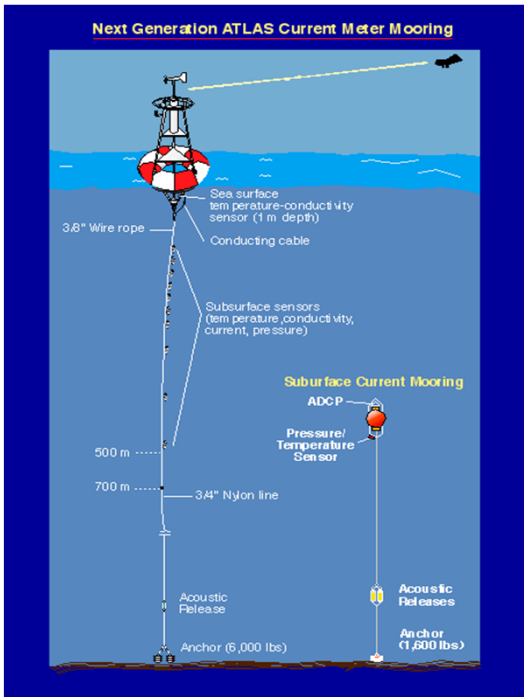

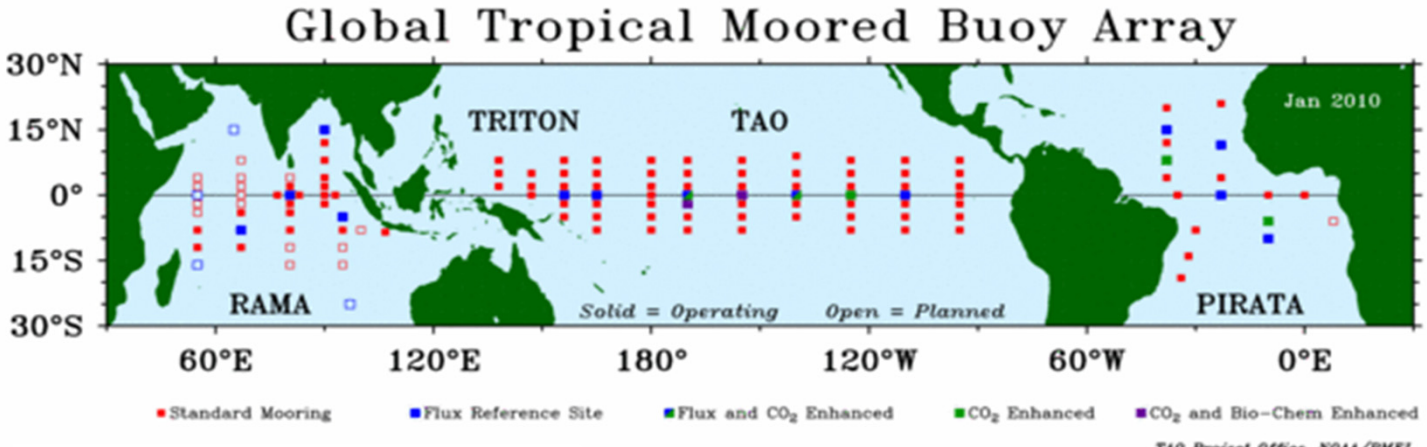

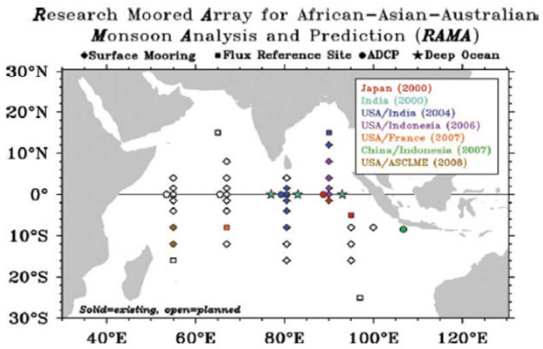

FIG. 4. Schematic of RAMA as of Dec 2008. Filled symbols indicate occupied sites. Color coding indicates national support, with year of first involvement shown in the upper-right box. Open symbols indicate sites not yet instrumented. ASCLME is a consortium of nine African nations including Kenya, Tanzania, Mozambique, South Africa, Madagascar, Mauritius, Seychelles, Somalia, and Comoros.

McPhaden et al., 2009 (BAMS)

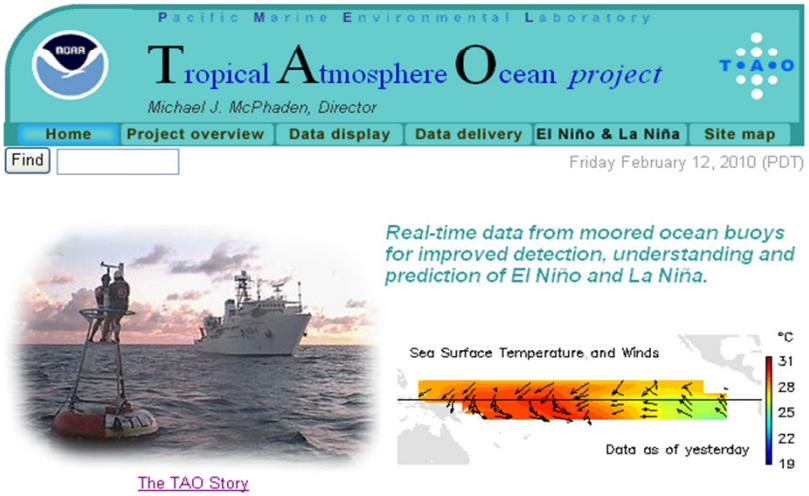

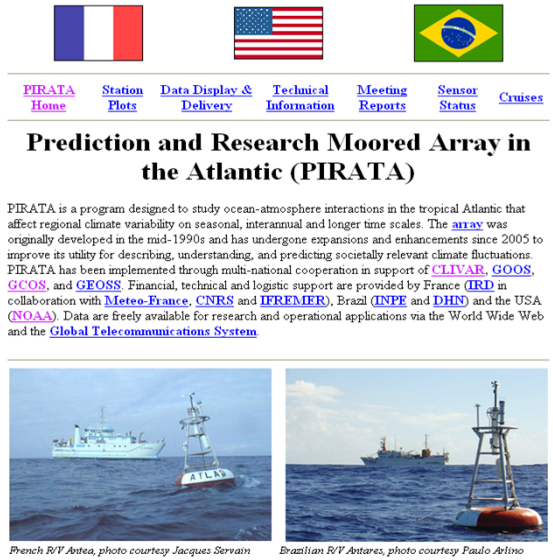

ENSO Mechanism

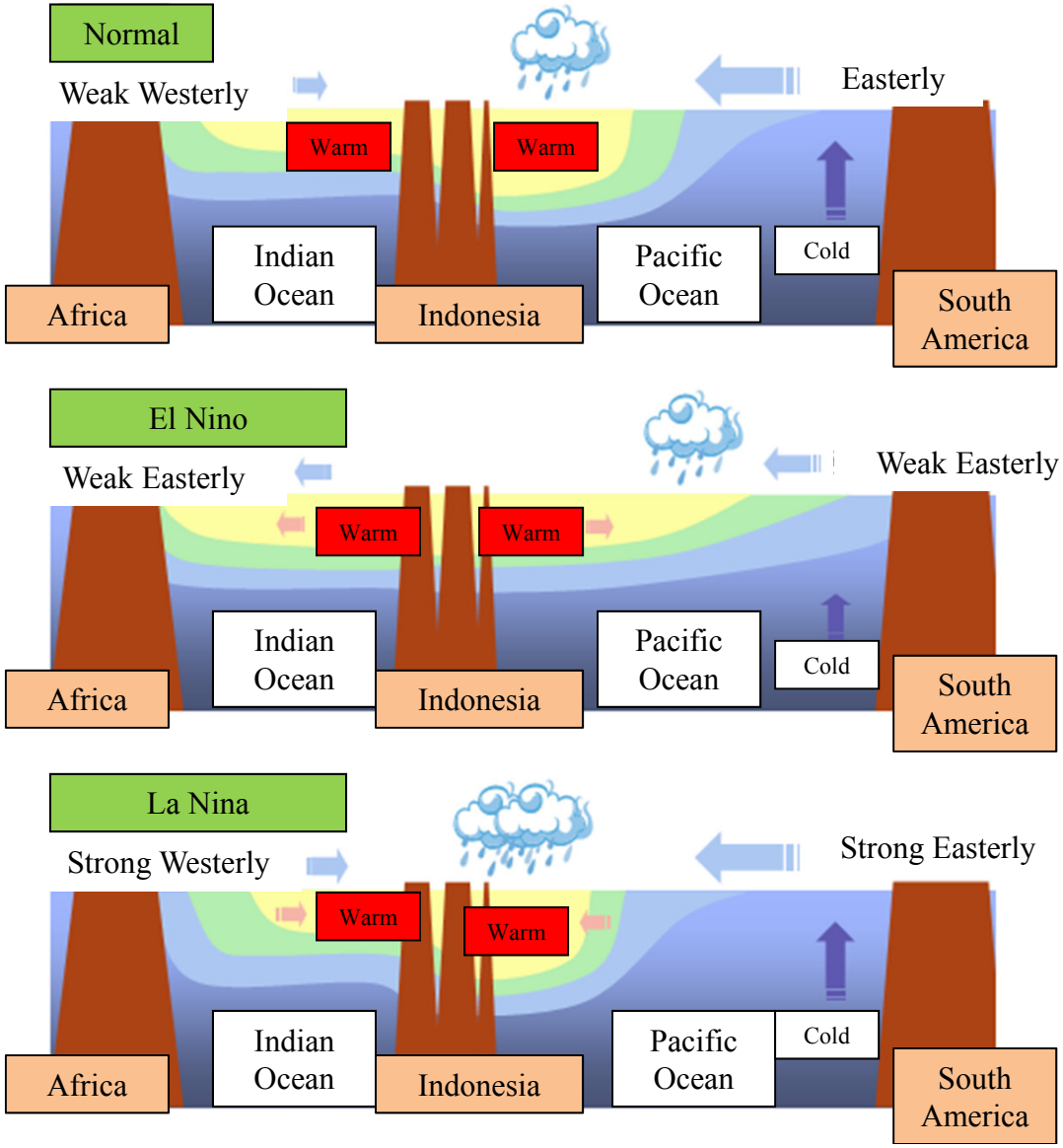

from JMA website

ENSO 1997/98

NOAA/PMEL

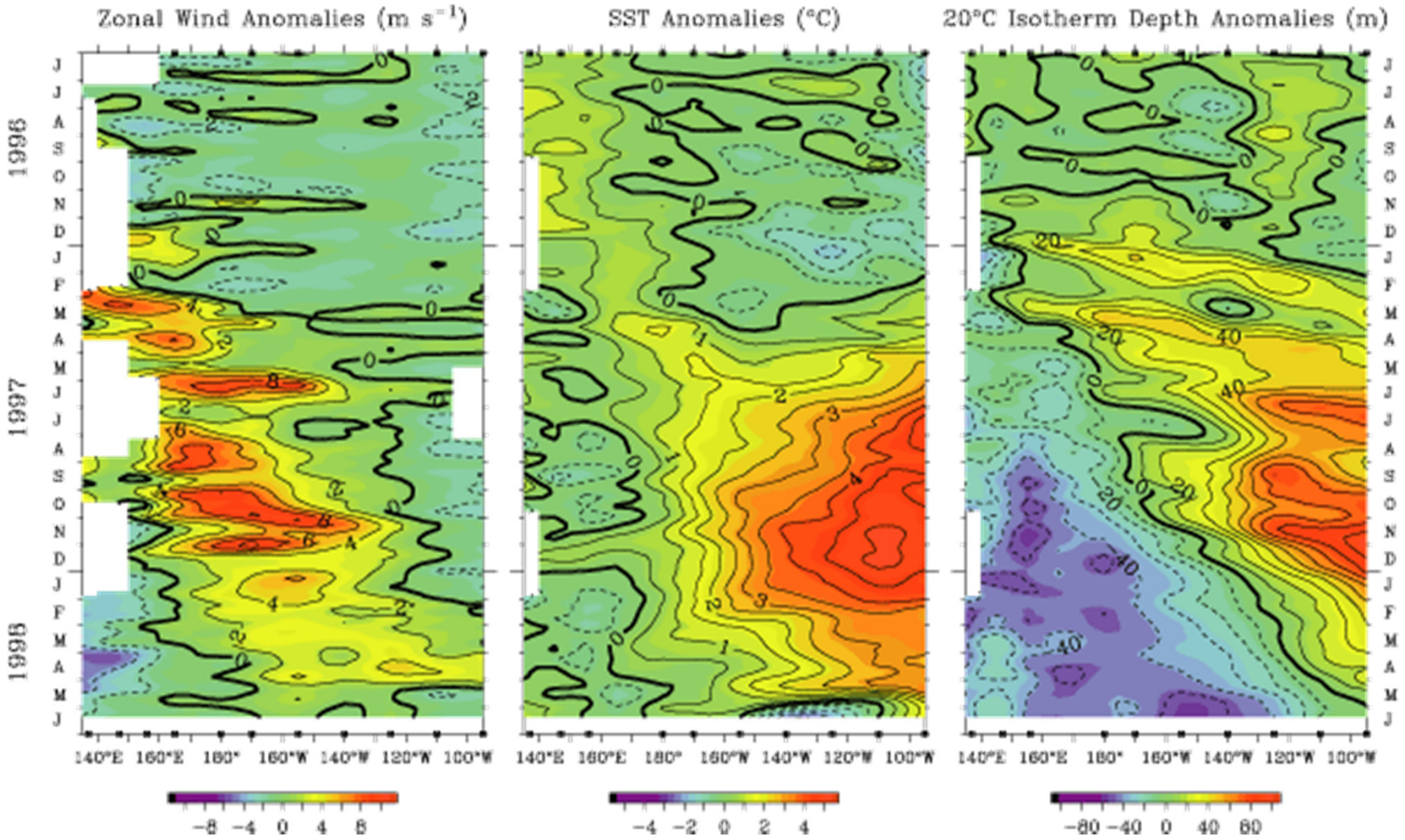

Time-longitude sections of anomalies in the surface zonal winds (m/sec), SST (° C) and 20° C isotherm depth (m) for the 24 months. Analysis is based on 5-day averages between 2° N-2° S of moored time series from the TAO array. Anomalies are relative to monthly climatologies cubic spline fitted to 5-day intervals (COADS winds, Reynolds SST, CTD/XBT 20° C depths).

ENSO transition

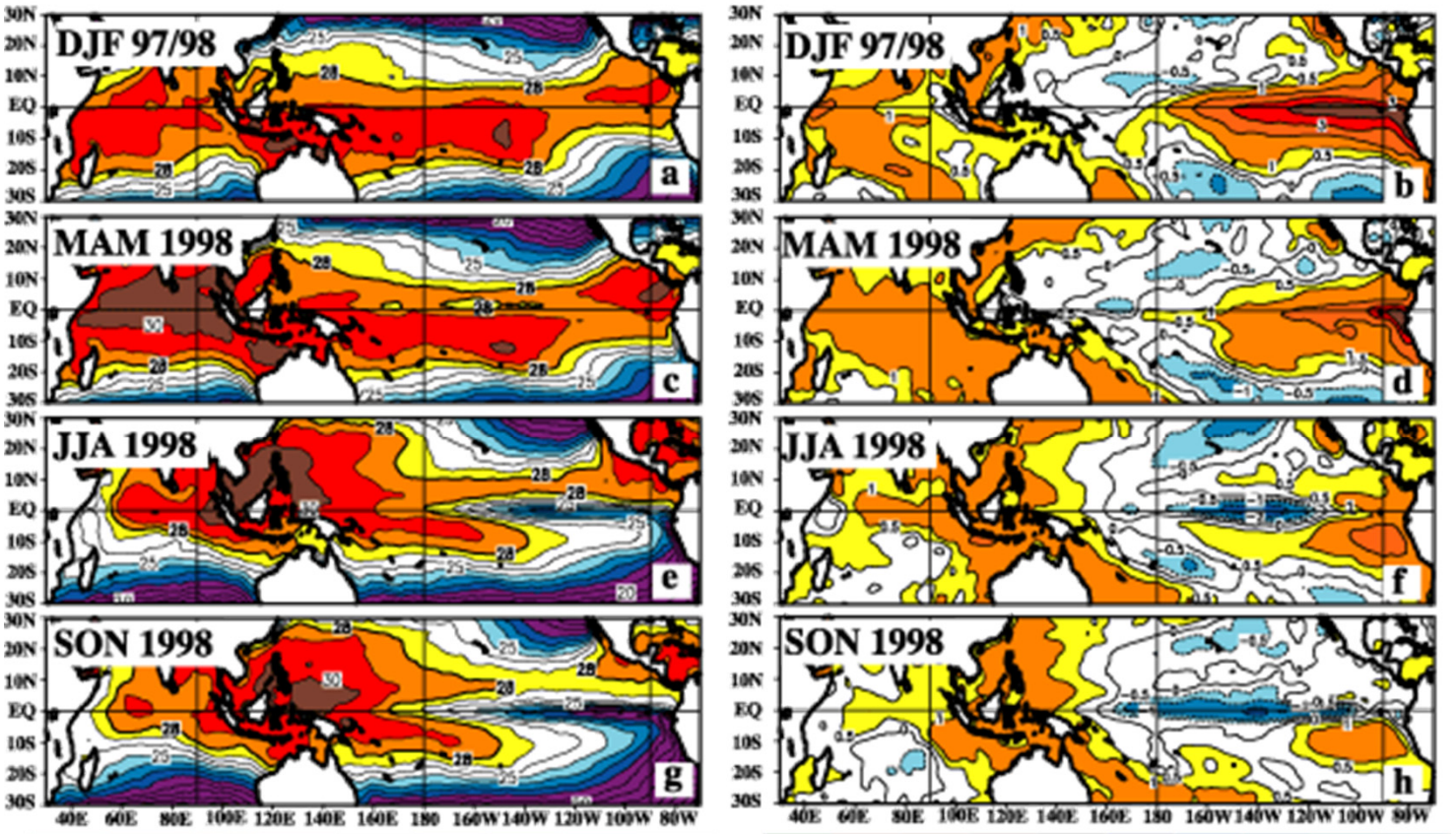

Seasonal SST (left) and anomaly (right) for DJF 1997/98, MAM 1998, JJA 1998, SON 1998. Contour interval is 1° C, with the 0.5° C contour included. Anomalies are departures from the 1950-79 adjusted OI climatology (Reynolds and Smith 1995) (from BAMS, 1999, 80, S1-48)

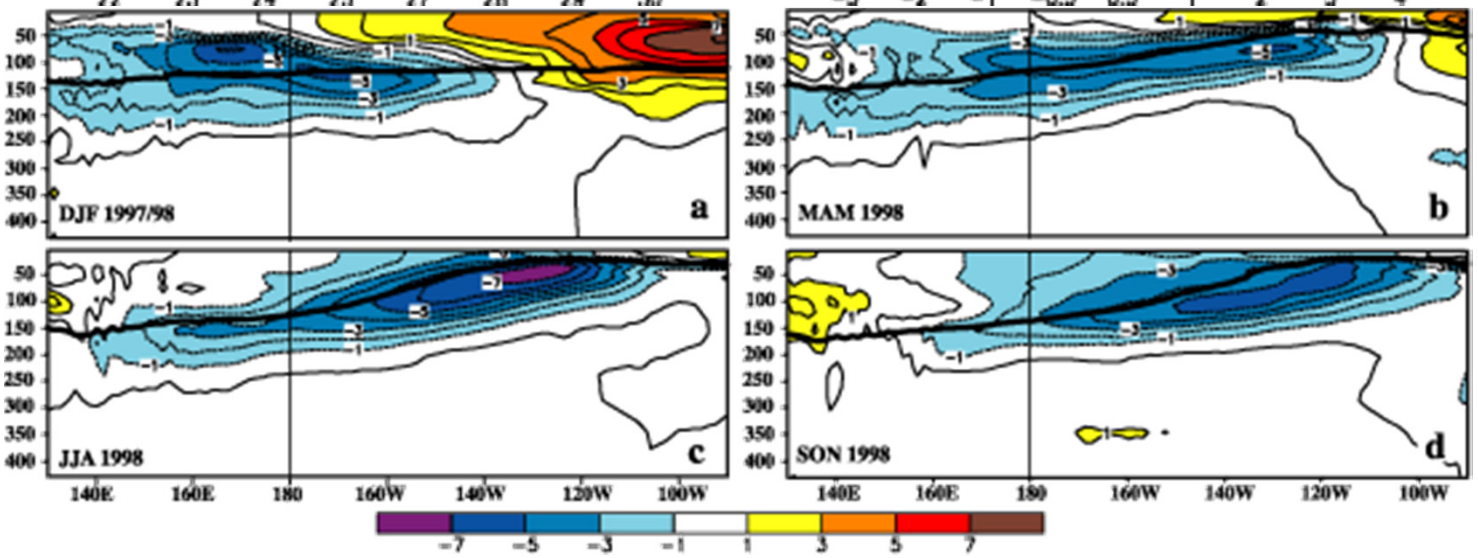

Equatorial depth-longitude section of ocean temperature anomalies. Contour interval is 1(C. The dark line is 208C isotherm. Data are derived from an analysis system that assimilates oceanic observations into an oceanic GCM (Behringer et al. 1998). Anomalies are departures from the 1983-92 base period means.

Rainfall anomalies during November 1997-April 1998

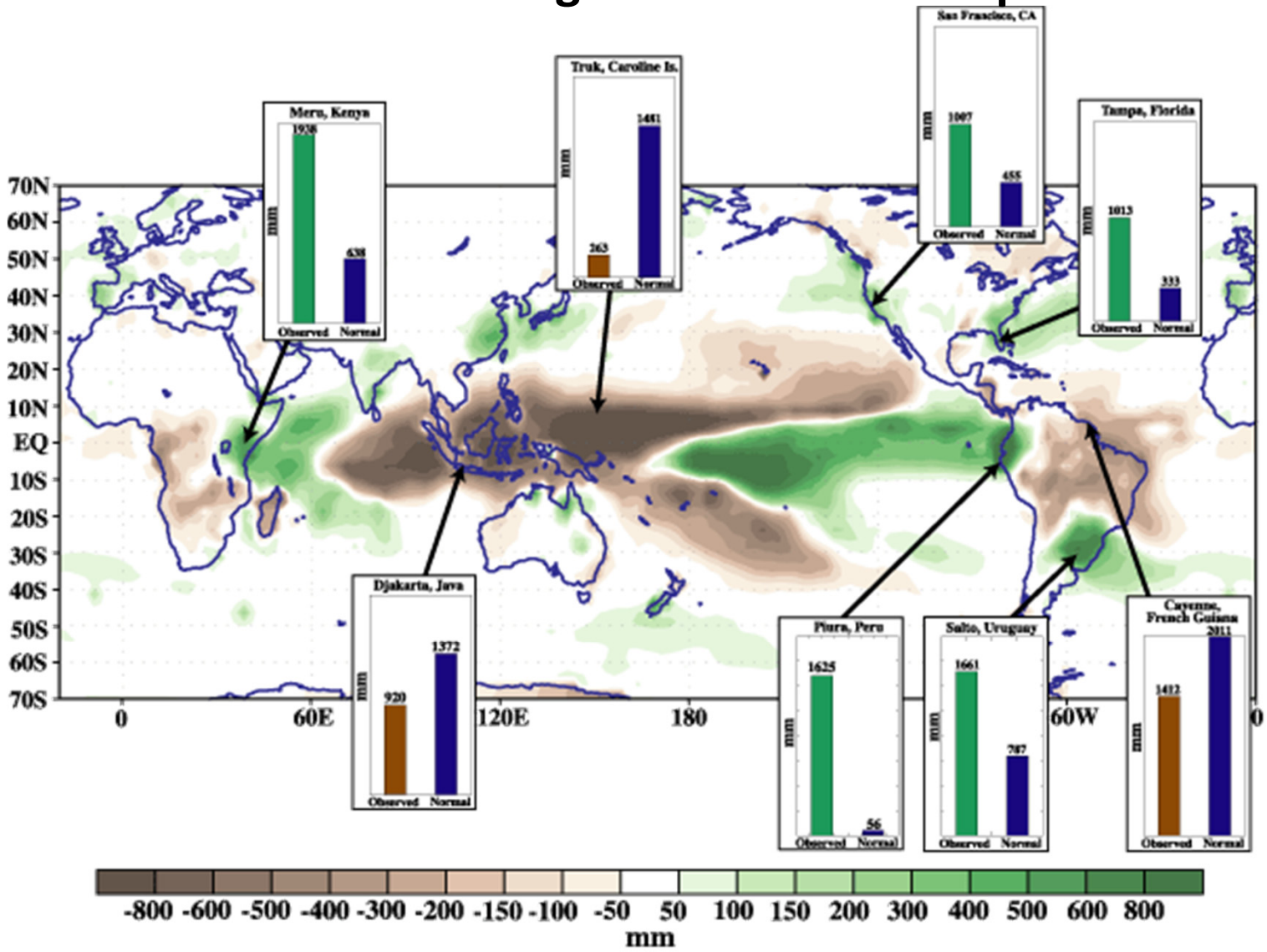

Accumulated rainfall departures during November 1997-April 1998. Precipitation amounts are obtained by merging rain gauge observations and satellite-derived precipitation estimates. The satellite estimates are generated by the outgoing longwave radiation precipitation technique (Xie and Arkin 1998), and are merged with rain gauge data via a method adapted from Xie and Arkin (1996). Anomalies are departures from the 1979-95 base period means (from BAMS, 1999, 80, S1-48).

Correlation coefficient map
between Rainfall anomalies and Nino3.4 SST anomaly

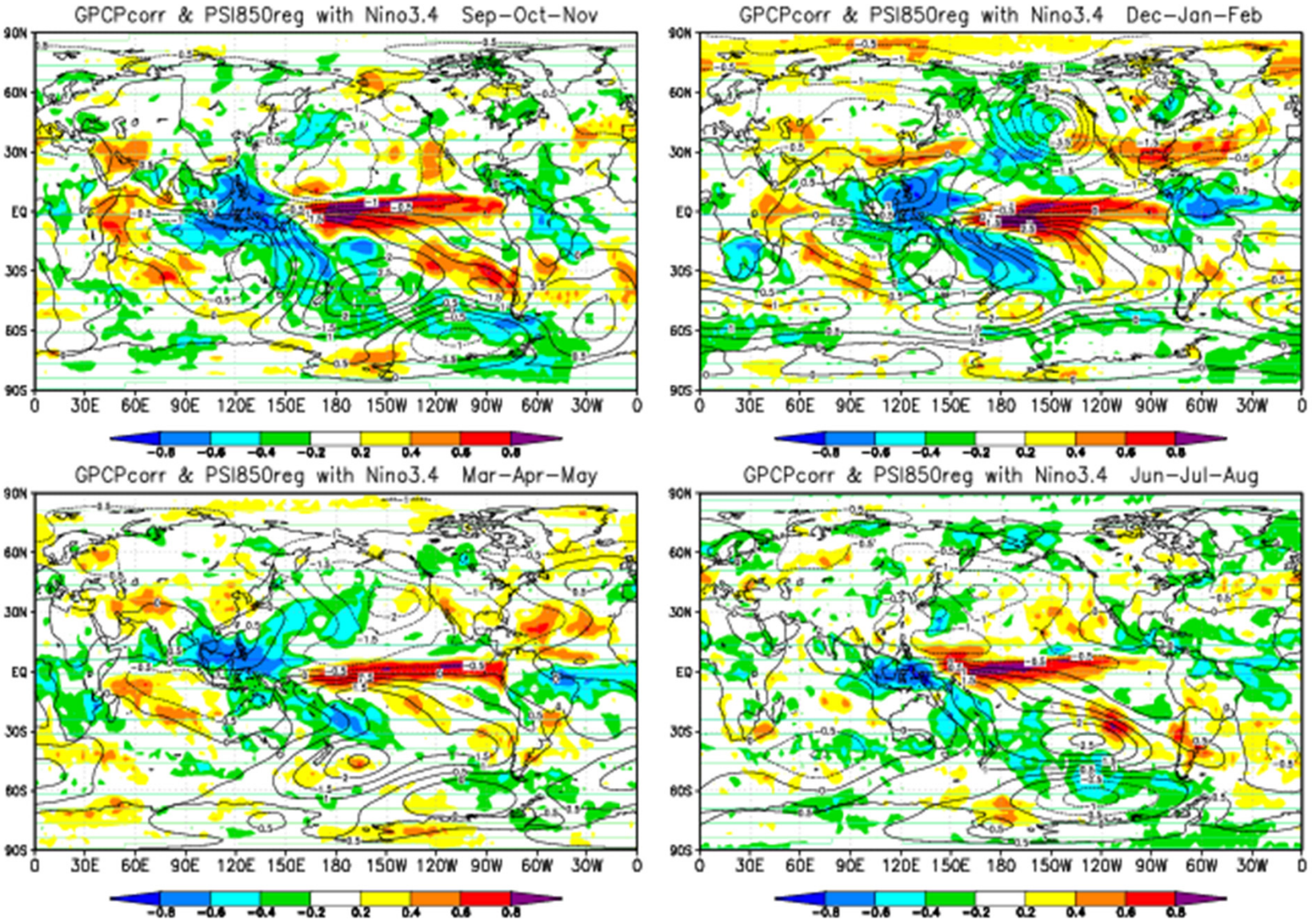

Correlation coefficient map
between 850hPa temperature anomalies and Nino3.4 SST anomaly

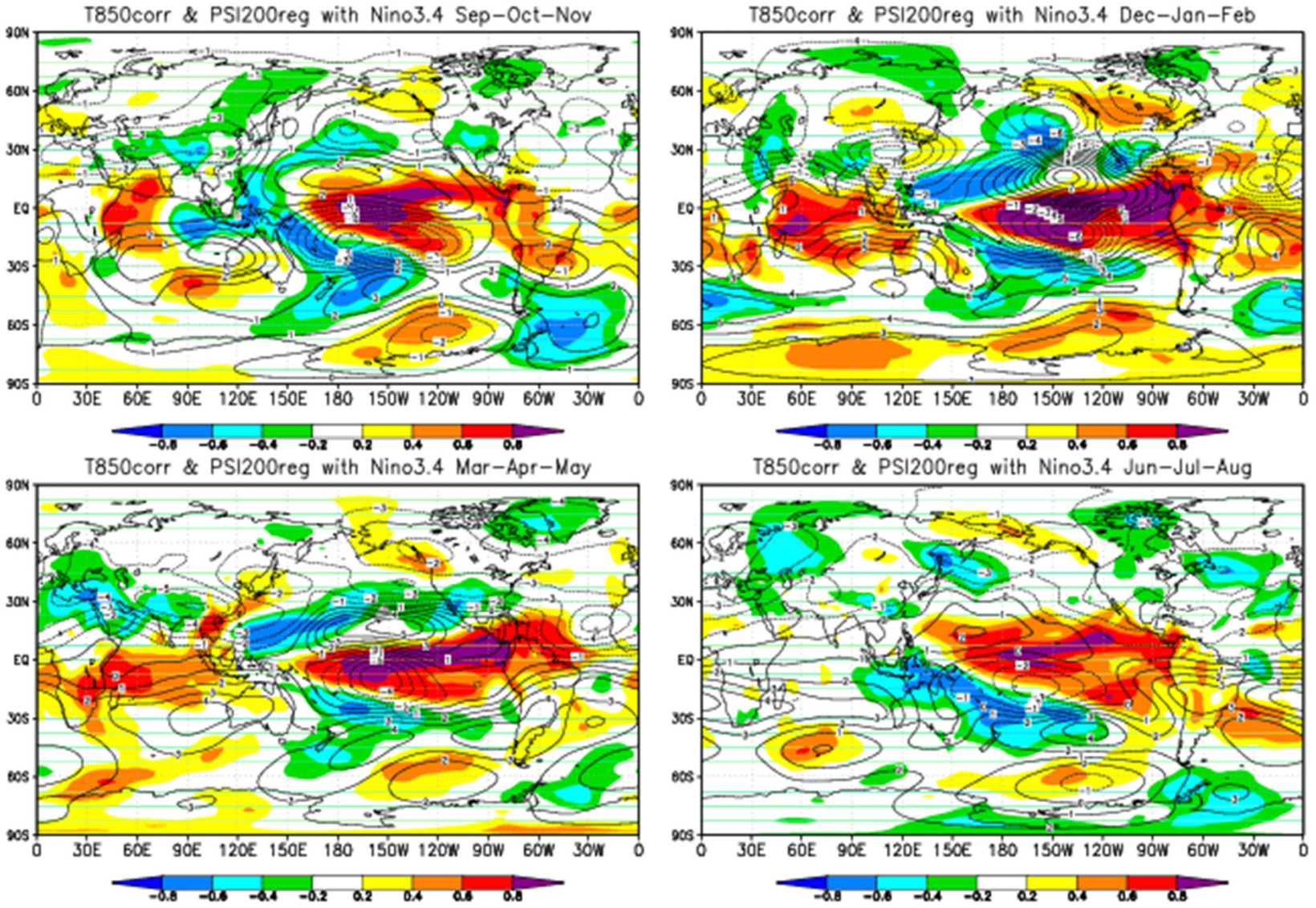

Nature,2009

The El Niño with a difference

Karumuri Ashok and Toshio Yamagata

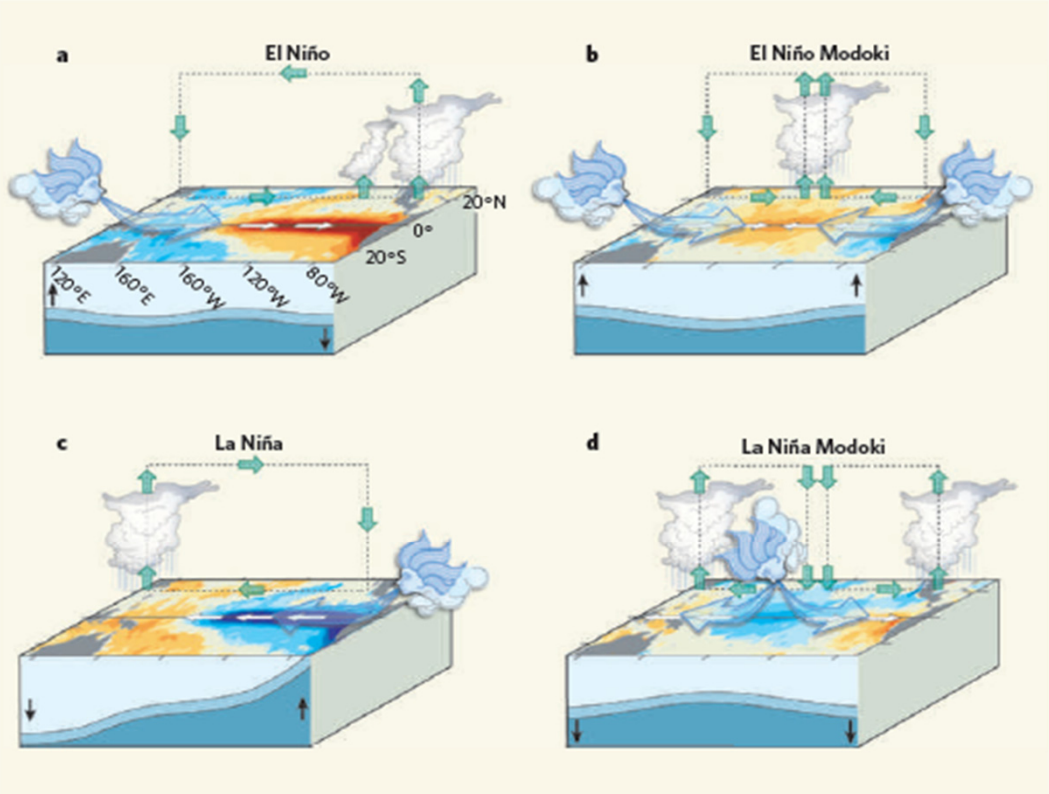

Figure 2 | Anomalous conditions in the tropical Pacific. **a**, An El Niño event is produced when the easterly winds weaken; sometimes, in the west, westerlies prevail. This condition is categorized by warmer than normal sea surface temperatures (SSTs) in the east of the ocean, and is associated with alterations in the thermocline and in the atmospheric circulation that make the east wetter and the west drier. **b**, An El Niño Modoki event is an anomalous condition of a distinctly different kind. The warmest SSTs occur in the central Pacific, flanked by colder waters to the east and west, and are associated with distinct patterns of atmospheric convection. **c**, **d**, The opposite (La Niña) phases of the El Niño and El Niño Modoki respectively. Yeh *et al.*[3] argue that the increasing frequency of the Modoki condition is due to anthropogenic warming, and that these events in the central Pacific will occur more frequently if global warming increases.

Nature,2009

El Niño in a changing climate

Sang-Wook Yeh[1], Jong-Seong Kug[1], Boris Dewitte[2], Min-Ho Kwon[3], Ben P. Kirtman[4] & Fei-Fei Jin[3]

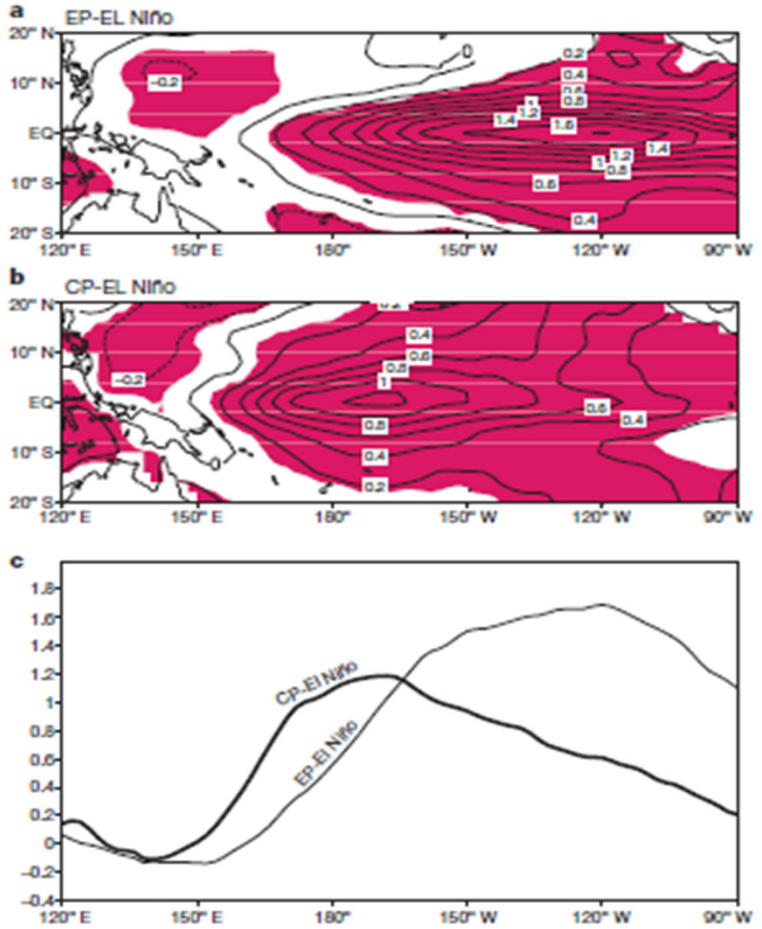

Figure 1 | Deviations of mean SST for the two characteristics of El Niño from the 1854–2006 climatology. **a**, The EP-El Niño; **b**, the CP-El Niño. The contour interval is 0.2 °C and shading denotes a statistical confidence at 95% confidence level based on a Student's *t*-test. **c**, The zonal structure for the composite EP-El Niño (thin line) and CP-El Niño (thick line) averaged over 2 °N to 2 °S.

Anomalous winter climate conditions in the Pacific rim during recent El Niño Modoki and El Niño events

Hengyi Weng , Swadhin K. Behera and Toshio Yamagata

(Climate Dynamics, 32, 663-674, 2009)

Regressed SST&skin-temperature (Jan-Feb-Mar)	Regressed rainfall & surface wind (Jan-Feb-Mar)

Nino3

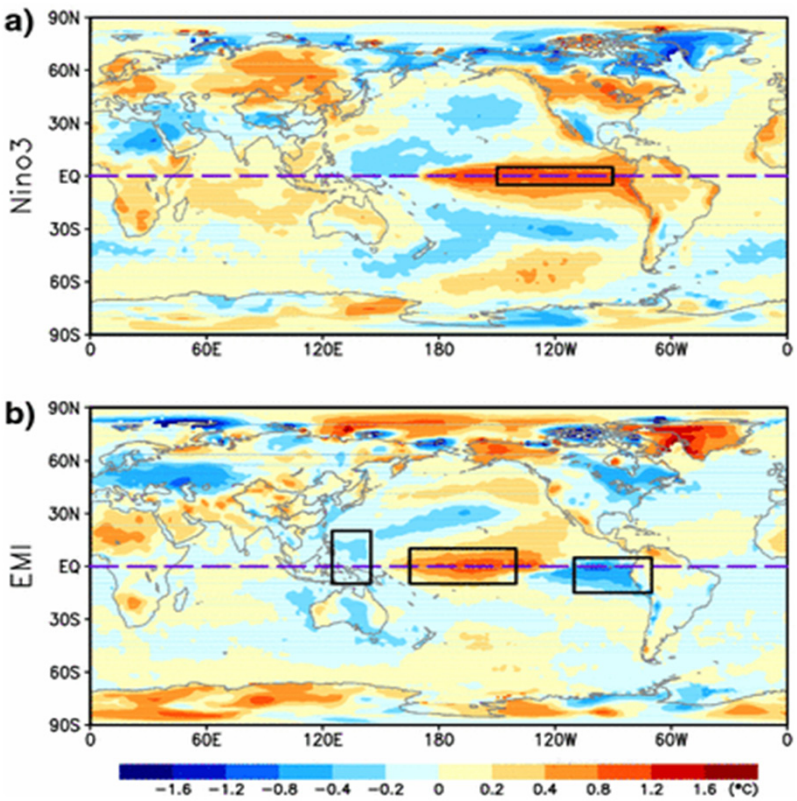

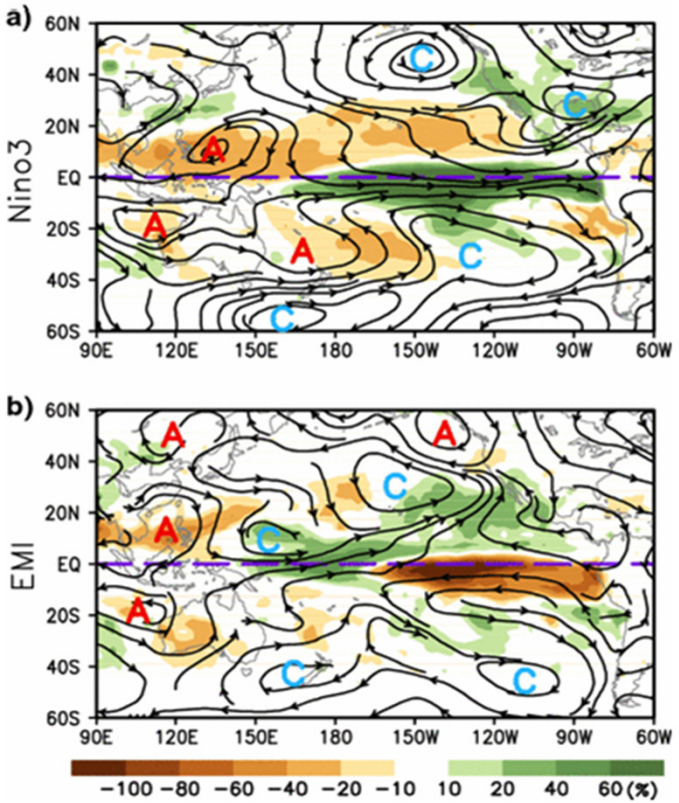

EMI = SSTA(C)-0.5*SSTA(W)-0.5*SSTA(E)

Science, 2006

Unraveling the Mystery of Indian Monsoon Failure During El Niño

K. Krishna Kumar,[1] Balaji Rajagopalan,[2,3] Martin Hoerling,[4*] Gary Bates,[4] Mark Cane[5]

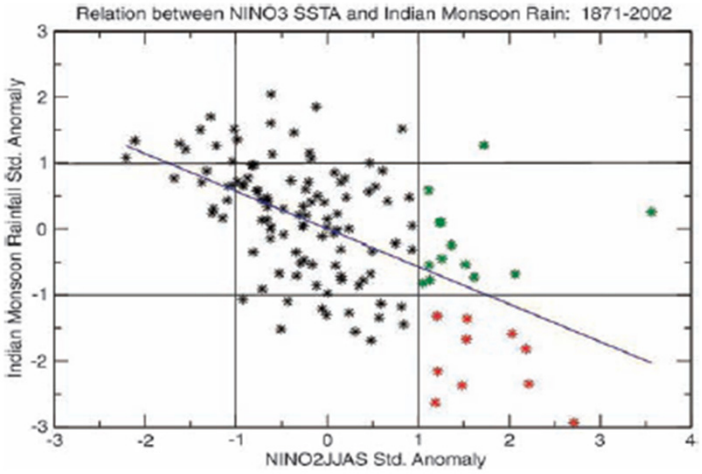

Fig. 1. Plot of standardized, all-India summer [June to September (JJAS)] monsoon rainfall and summer NINO3 anomaly index. Severe drought and drought-free years during El Niño events (standardized NINO3 anomalies > 1) are shown in red and green, respectively.

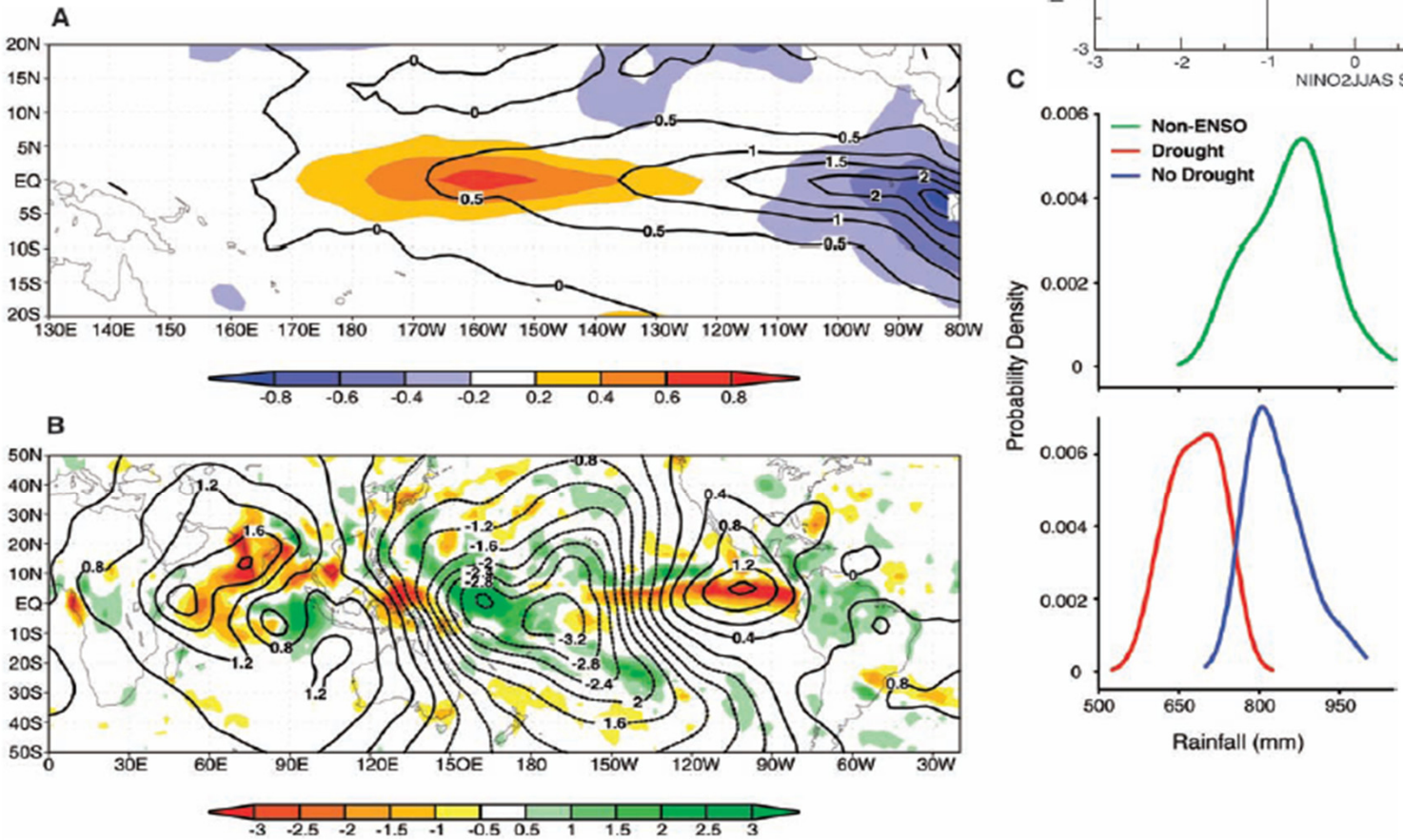

Fig. 2. (**A**) Composite SST difference pattern between severe drought (shaded) and drought-free El Niño years. Composite SST anomaly patterns of drought-free years are shown as contours. (**B**) Composite difference pattern between severe drought and drought-free years of velocity potential (contours) and rainfall (shaded). (**C**) PDF of all-India summer monsoon rainfall from severe-drought (red curve) and drought-free (blue curve) years associated with El Nino occurrence and from the non-ENSO years (green curve). SST and velocity potential composite differences are based on 1950 to 2004, rainfall composites are based on 1979 to 2004, and PDFs are based on 1873 to 2004.

Unraveling the Mystery of Indian Monsoon Failure During El Niño

Science, 2006

K. Krishna Kumar,[1] Balaji Rajagopalan,[2,3] Martin Hoerling,[4]* Gary Bates,[4] Mark Cane[5]

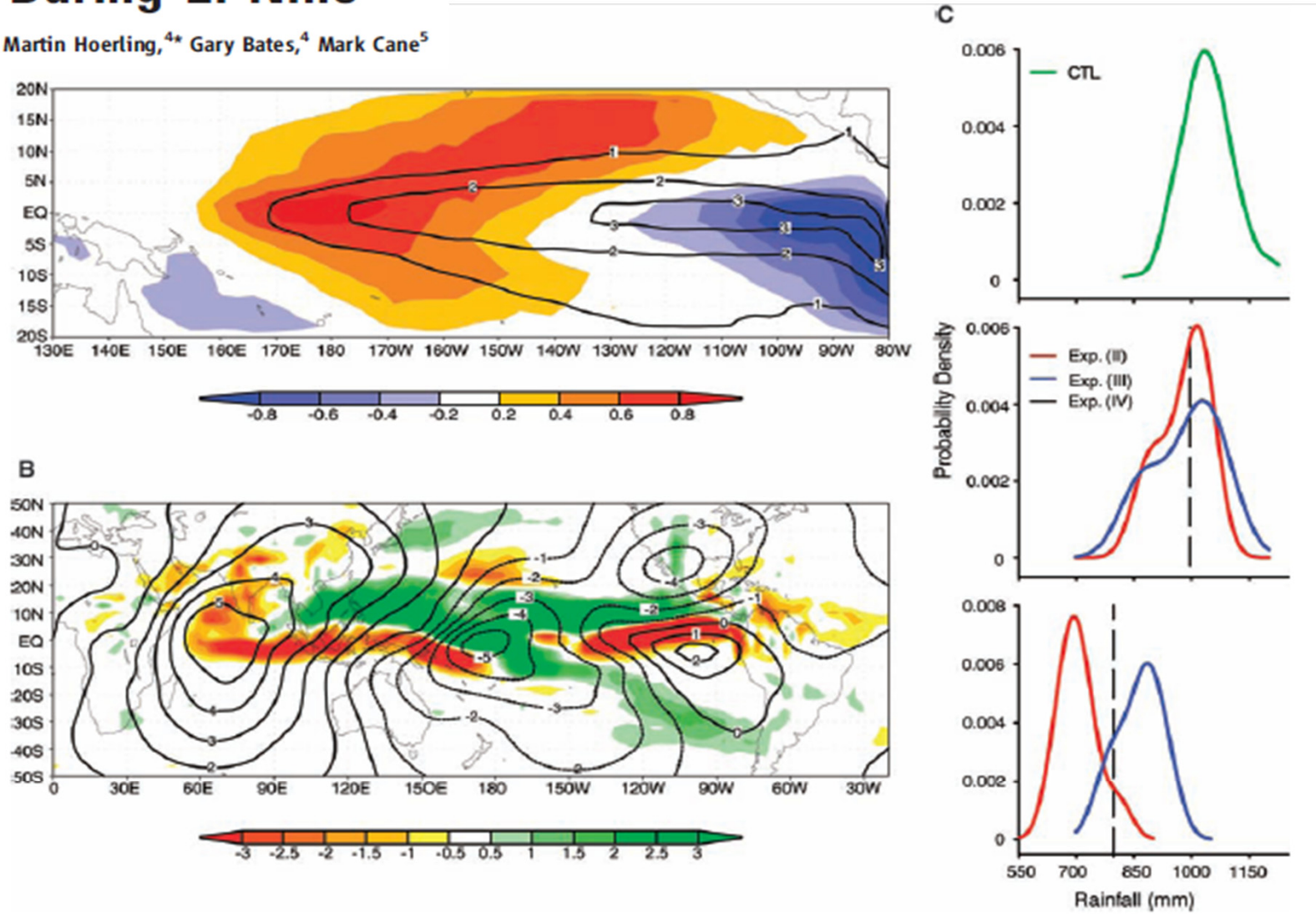

Fig. 4. (**A**) Contours are of the +2 SD experiment (iii) and are analogous to the amplitude and structure of the composite El Niño SSTs for drought-free years in Fig. 2A. Shadings are of the difference between the +2 SD SST forcings of experiments (ii) and (iii) and are analogous to the observed SST structure that discriminates severe drought from drought-free El Niño years. (**B**) The ensemble mean rainfall (shading) and 200 hPa velocity potential (contour) differences between experiments (ii) and (iii). (**C**) The PDF of the Indian monsoon rainfall corresponding to (top) the control, or unforced, experiment (i) green curve; and (middle and bottom) the forced experiments (ii) red curve, (iii) blue curve, and (iv) dashed line with +1 SD (middle) and +2 SD (bottom) imposed SST anomalies. For forced experiment (iv), only the median value (dashed line) is shown. For the forced experiments, each PDF is estimated from 30 ensembles. The model rainfall has been averaged over the Indian monsoon region of 8° to 30°N, 70° to 90°E.

Indian Ocean Capacitor Effect on Indo–Western Pacific Climate during the Summer following El Niño

SHANG-PING XIE,*,+ KAIMING HU,# JAN HAFNER,* HIROKI TOKINAGA,* YAN DU,*,@
GANG HUANG,# AND TAKEAKI SAMPE*

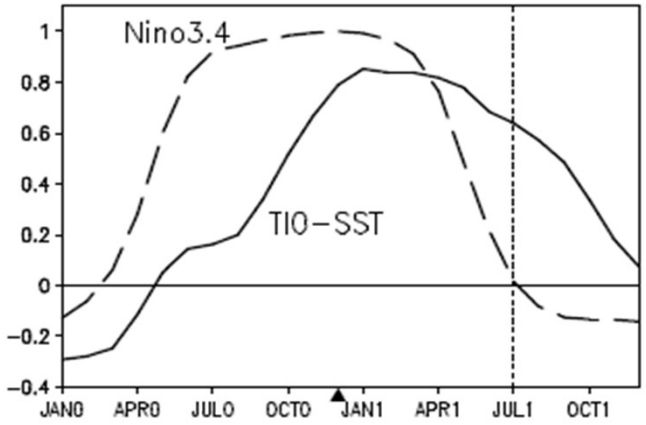

Fig. 1. Correlation of tropical Indian Ocean (40-100°E, 20°S-20°N) SST (solid) with the Nino3.4 (170°W-120°W, 5°S-5°N) SST index for Nov(0)-Dec(0)-Jan(1). Numerals in parentheses denote years relative to El Nino: 0 for its developing and 1 for decay year. The dashed curve is the Nino3.4 SST auto-correlation as a function of lag. The black triangle denotes Dec(0), the peak phase of ENSO.

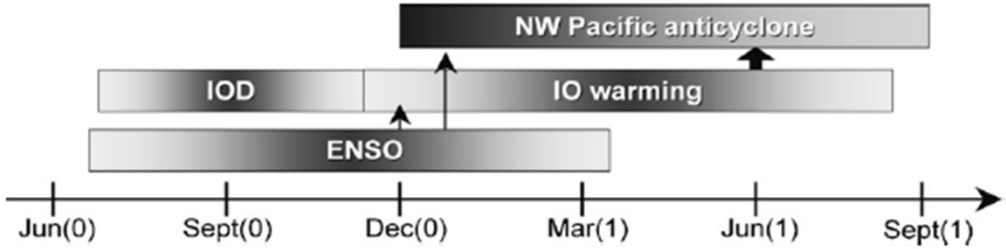

FIG. 13. Seasonality of major modes of Indo–western Pacific climate variability. Vertical arrows indicate causality, and the block arrow emphasizes the TIO capacitor effect, the major finding of the present study.

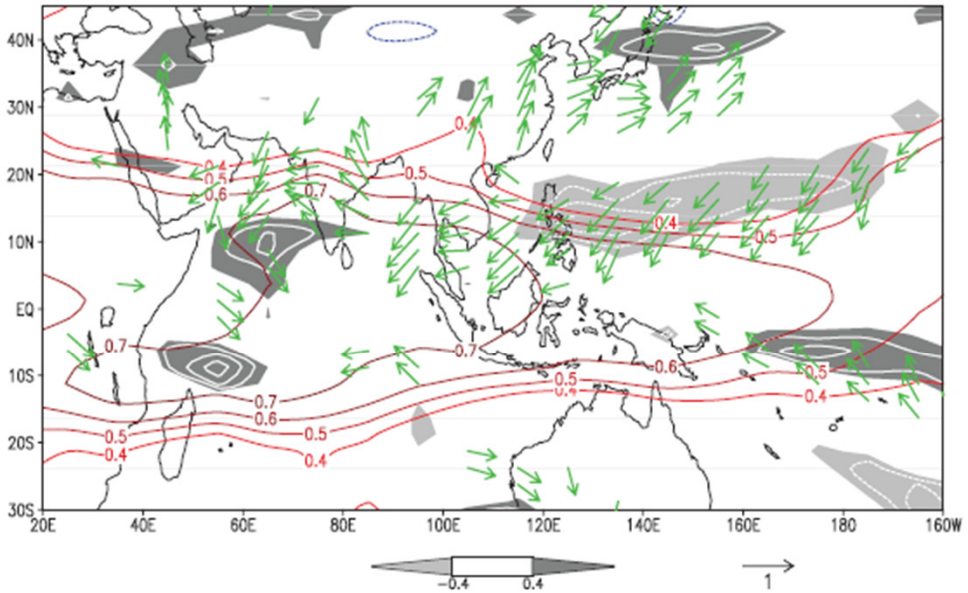

FIG. 6. JJA(1) correlation with the NDJ(0) Niño-3.4 SST index: tropospheric (850–250 hPa) temperature (contours), precipitation (white contours at intervals of 0.1; dark shade > 0.4; light < −0.4), and surface wind velocity (vectors).

A dipole mode in the tropical Indian Ocean

N. H. Saji*, B. N. Goswami†, P. N. Vinayachandran* & T. Yamagata*‡

Saji et al., Nature 1999

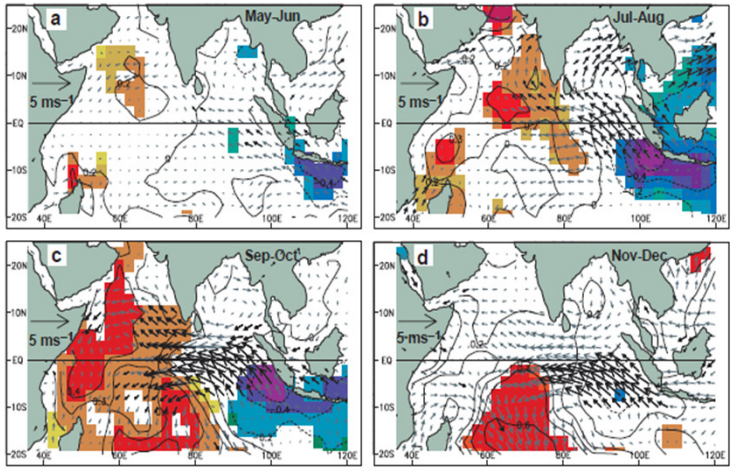

Figure 2 A composite dipole mode event. **a**–**d**, Evolution of composite SST and surface wind anomalies from May–June (**a**) to Nov–Dec (**d**). The statistical significance of the analysed anomalies were estimated by the two-tailed *t*-test. Anomalies of SSTs and winds exceeding 90% significance are indicated by shading and bold arrows, respectively.

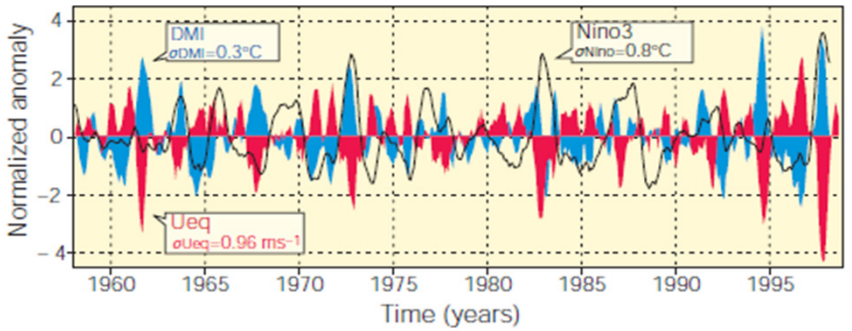

Figure 1 Dipole mode and El Niño events since 1958. Plotted in blue, the dipole mode index (DMI) exhibits a pattern of evolution distinctly different from that of the El Niño, which is represented by the Nino3 sea surface temperature (SST) anomalies (black line). On the other hand, equatorial zonal wind anomalies U_{eq} (plotted in red) coevolves with the DMI. All the three time series have been normalized by their respective standard deviations. We have removed variability with periods of 7 years or longer, based on harmonic analysis, from all the data sets used in this analysis. In addition, we have smoothed the time series using a 5-month running mean.

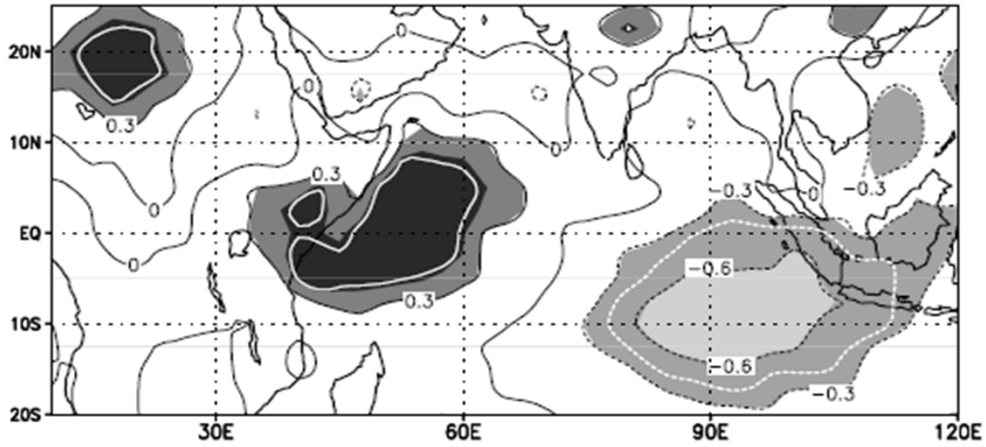

Figure 4 Rainfall shifts northwest of the OTCZ during dipole mode events. The map correlates the DMI and rainfall to illustrate these shifts. The areas within the white curve exceed the 90% level of confidence for non-zero correlation (using a two-tailed *t*-test).

Vol. 25: 151–169, 2003 | CLIMATE RESEARCH Clim Res | Published December 5

Possible impacts of Indian Ocean Dipole mode events on global climate

N. H. Saji[1,3,*], T. Yamagata[1,2]

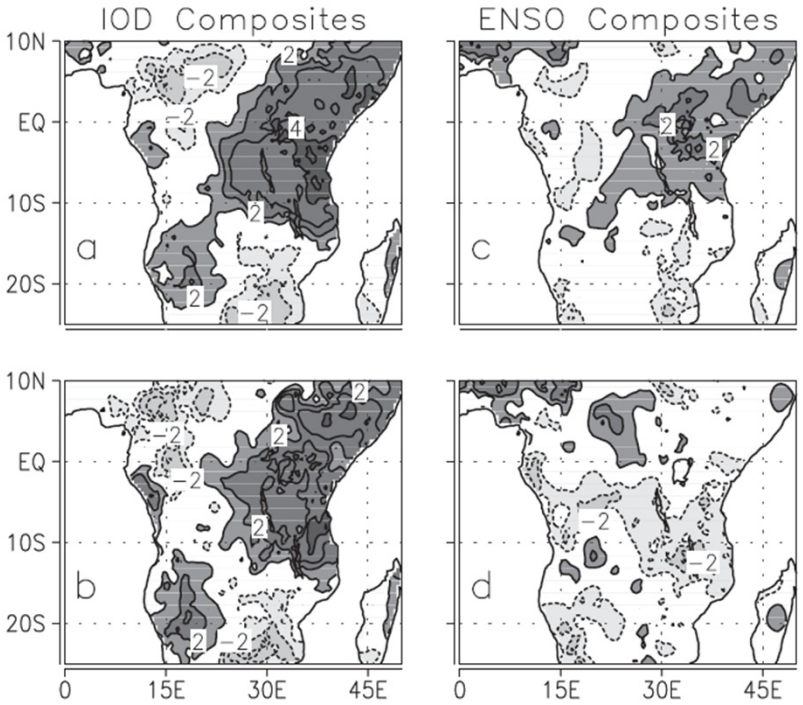

Fig. 1. Composite OND rain anomaly over Africa for (a) 19 IOD events, (b) 11 ENSO-independent IOD events, (c) 20 ENSO events and (d) 12 IOD-independent ENSO events. The composite anomaly was normalized by the standard deviation of rain during OND. Contours given at ±1, ±2, etc.

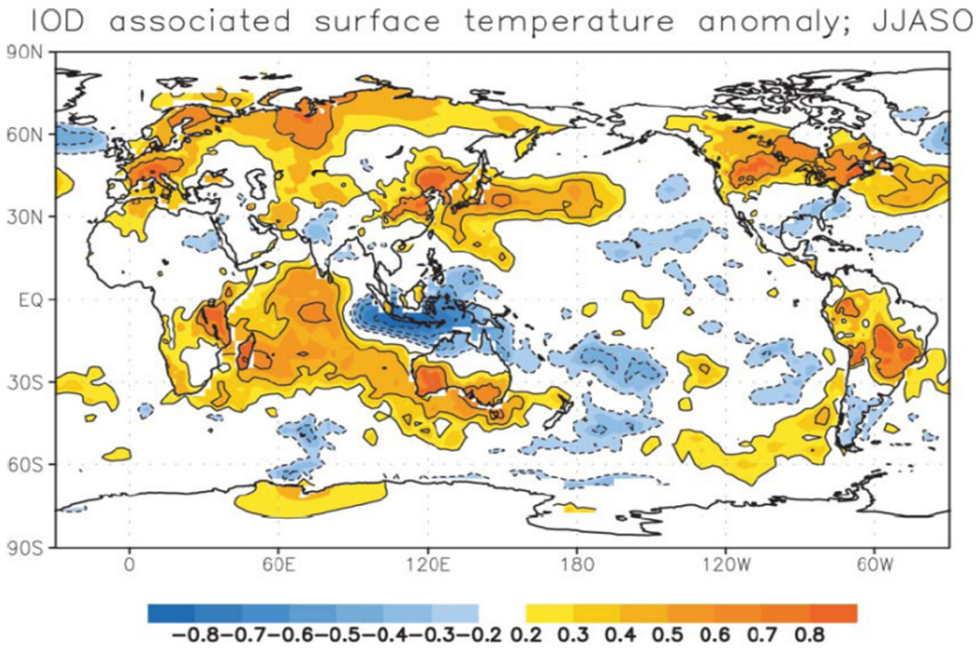

Fig. 21. Partial correlation of land and sea-surface temperature on DMI independent of Nino3 during JJASO

D1: The North Atlantic Oscillation

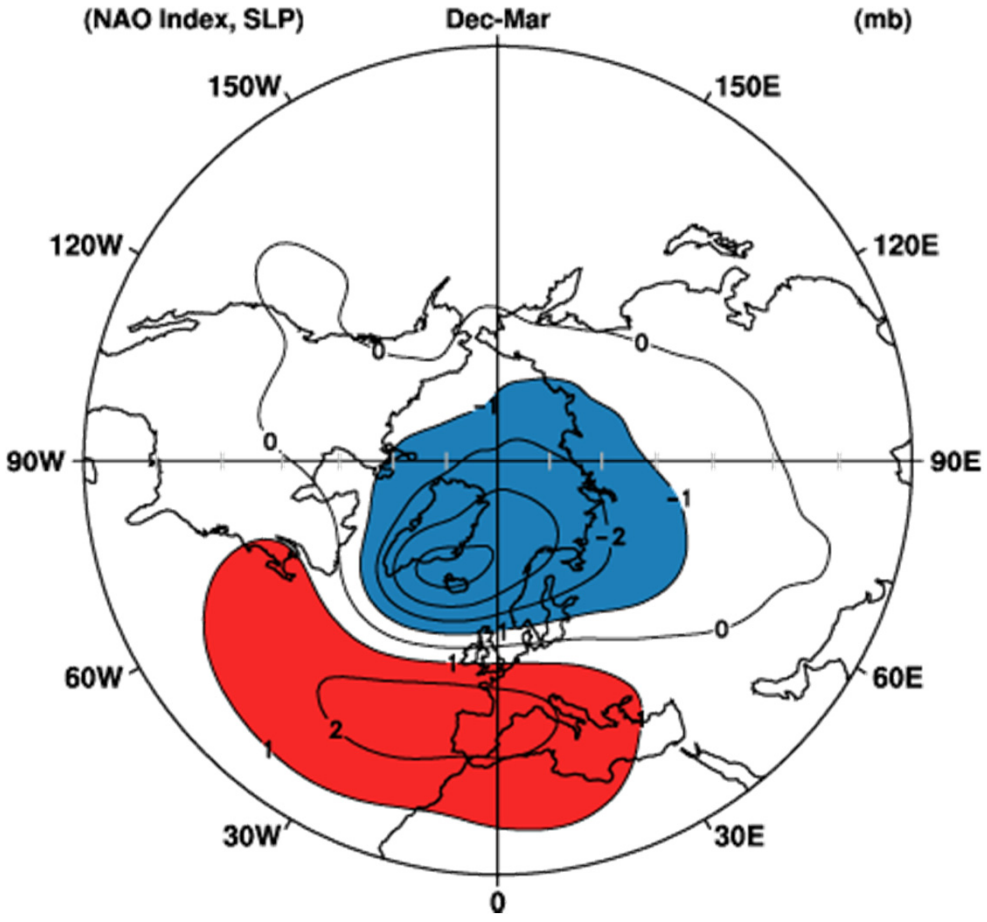

Observed Dec-Mar change in SLP associated with a 1 standard deviation in the NAO index (after Hurrell 1995).

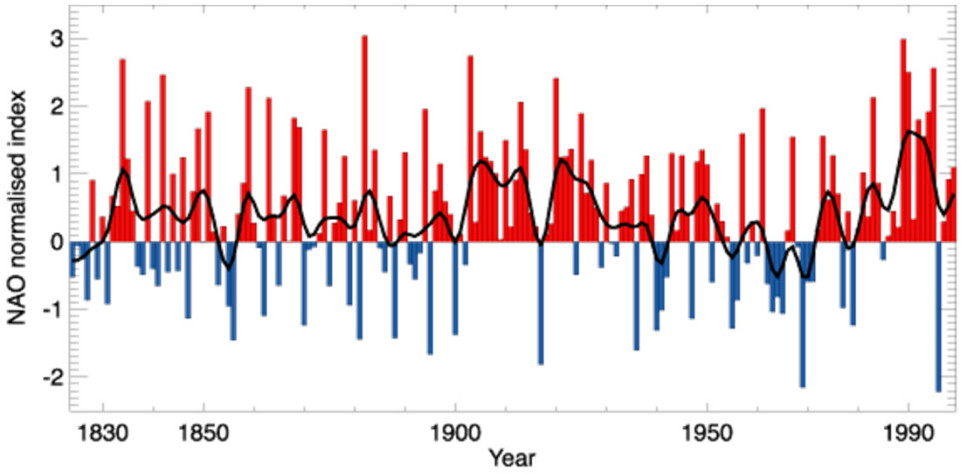

NAO index based on the difference of normalized SLP between Portugal and Iceland from 1864 to 1995.

The two phases of the NAO

CLIVAR AV/D1/99-1,99-2

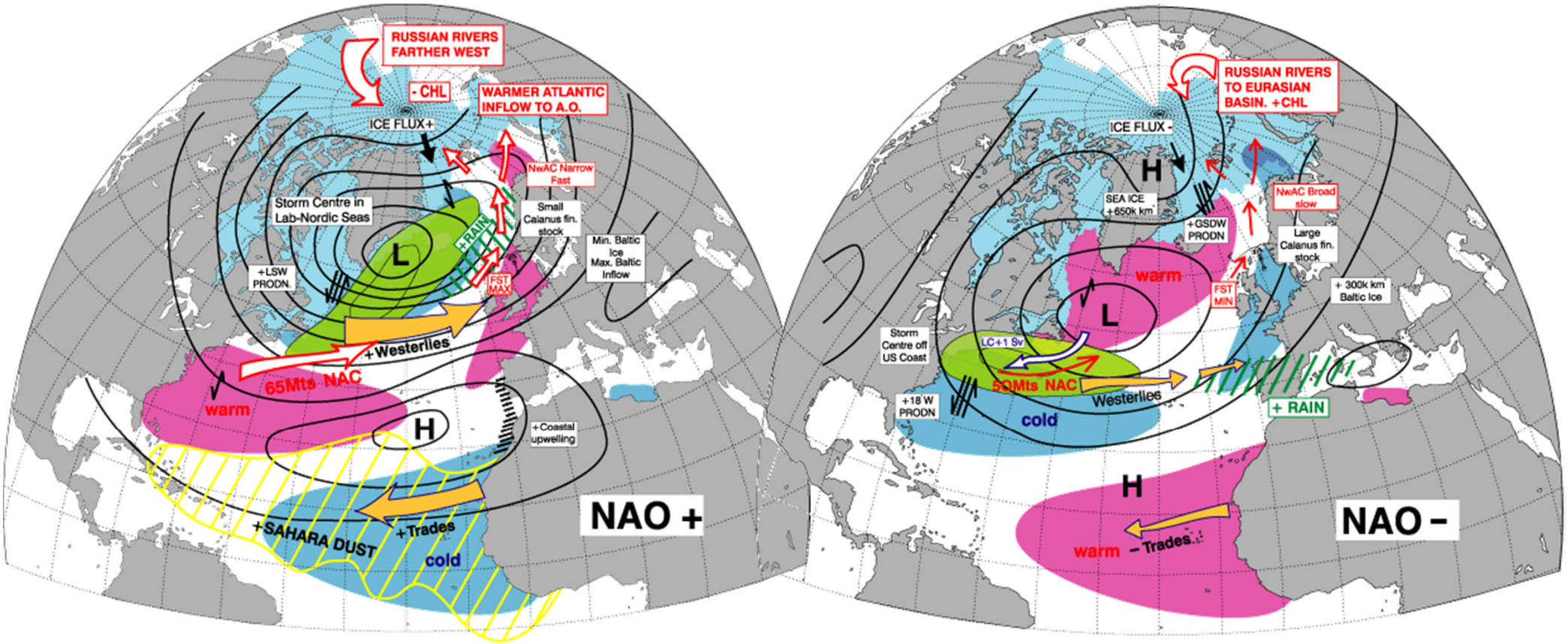

High phase: westerlies in the North Atlantic are enhanced, resulting in mild and wet winter conditions over Northern Europe

Low phase: westerlies in the North Atlantic are weakened, resulting in cold and dry winter conditions over Northern Europe

Impacts of the NAO

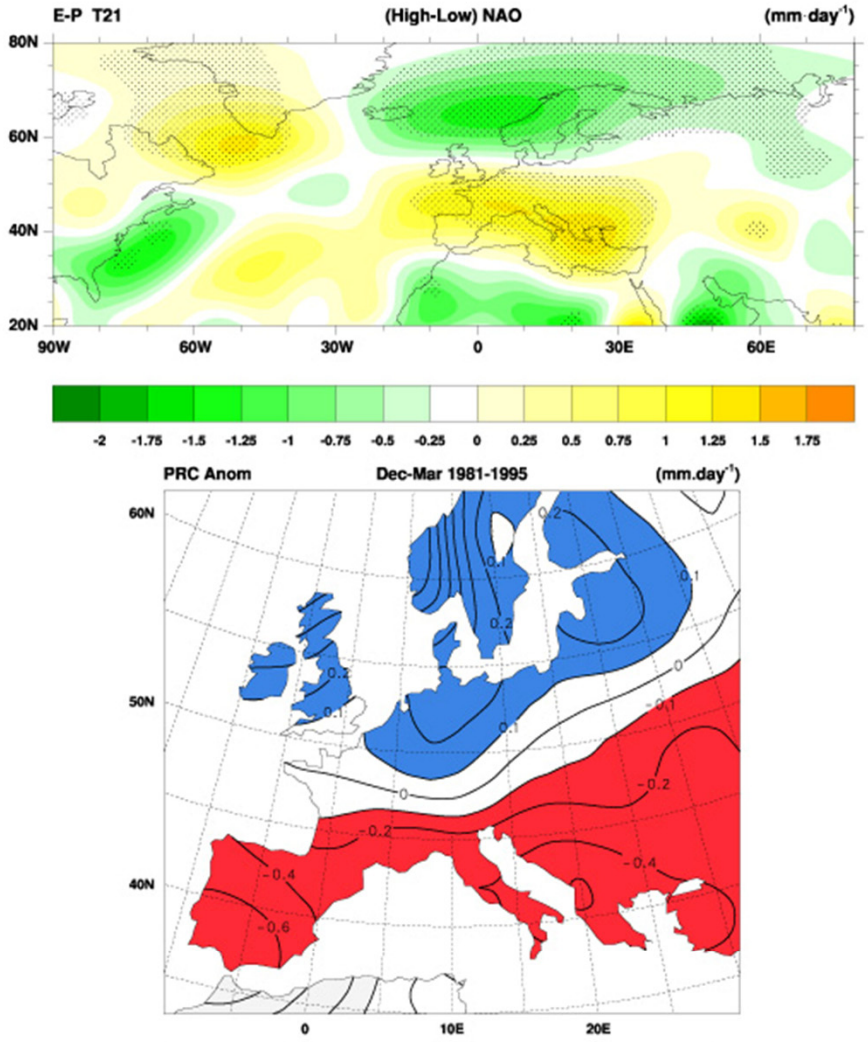

Upper panel: Above: Precipitation anomalies associated with the NAO; E-P is plotted, computed as a residual of the atmospheric moisture budget using ECMWF global analyses, for high NAO index minus low index winters (see Hurrell, 1995, Science, 269, 676-679).

Lower panel: Right: 1981-94 average precipitation anomalies expressed as departures from 1951-80 mean, from station data in Eischeid et al. (1991) data set (courtesy of J. Hurrell)

LB/D1/99-4

Impacts of the NAO

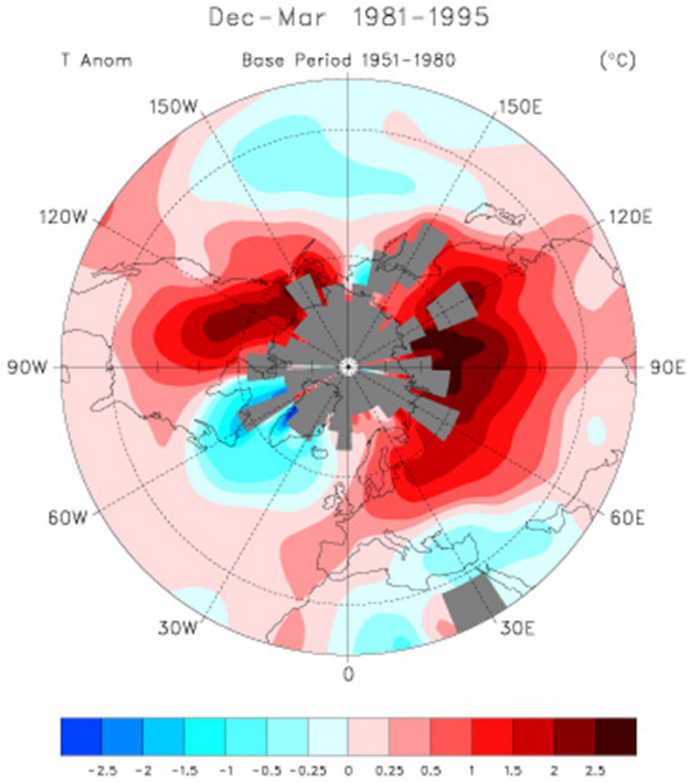

Observed Dec-March surface temperature anomalies associated with a high NAO index; the period 1981-1995, when the NAO was high, relative to the period 1951-1980, when the NAO was low (after Hurrell, 1996). The temperature data consists of land surface temperature blended with SST data (Jones and Briffa, 1992, The Holocene, 2, 174-188).

LB/D1/99-5

Current Seasonal Forecast is based on El Nino Predictability. (An Example of Four-month-lead Seasonal Prediction)

Observation (3-month Average from Dec. 1997 to Feb. 1998)

Model Prediction from Initials On 31 Jul. 1997

SST Anomaly

Precipitation Anomaly

Surface Air Temperature Anomaly

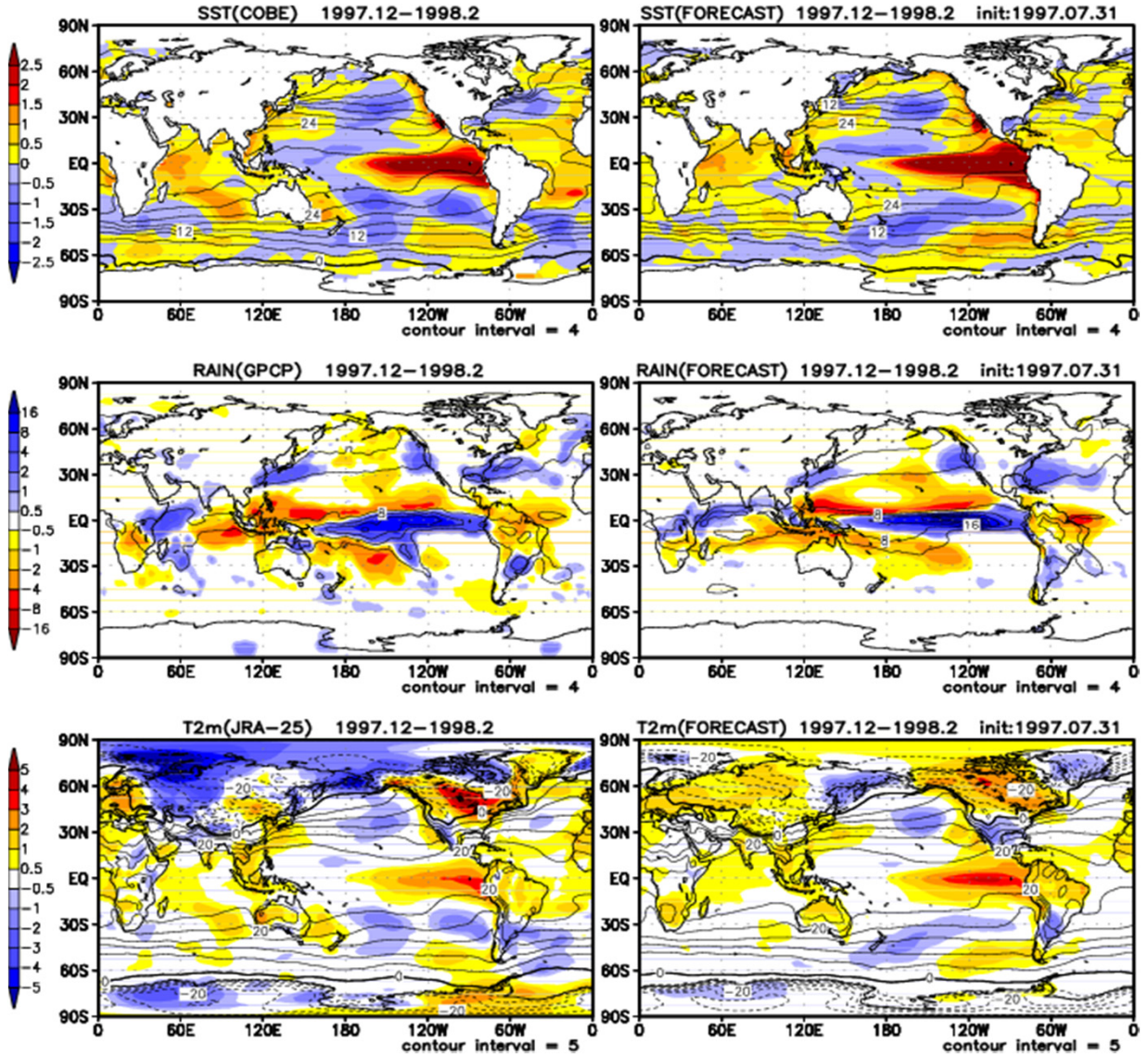

Four-month Lead Forecast

Precipitation predictions from the initials of Jan 31 over Southeast Asia

(115-140E, 10-20N)

ROC skill scores for upper tercile of precipitation prediction in Mar-May from the initials of Jan 31.

ROC skill scores for upper tercile of precipitation prediction in Jun-Aug from the initials of Jan 31.

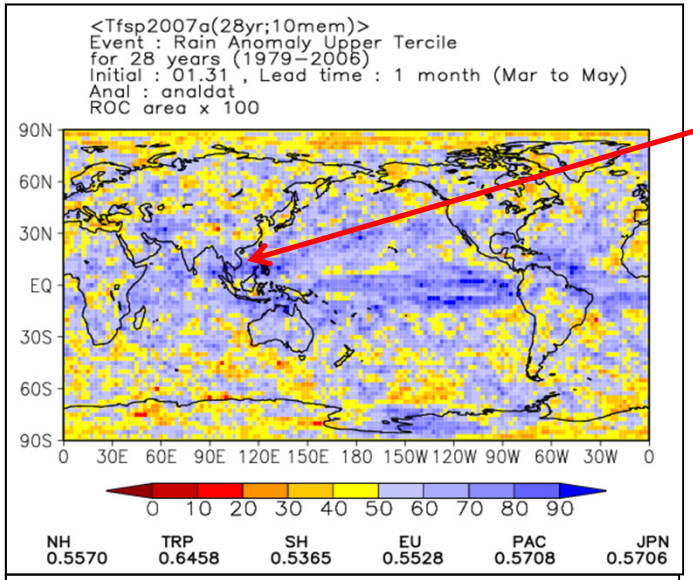

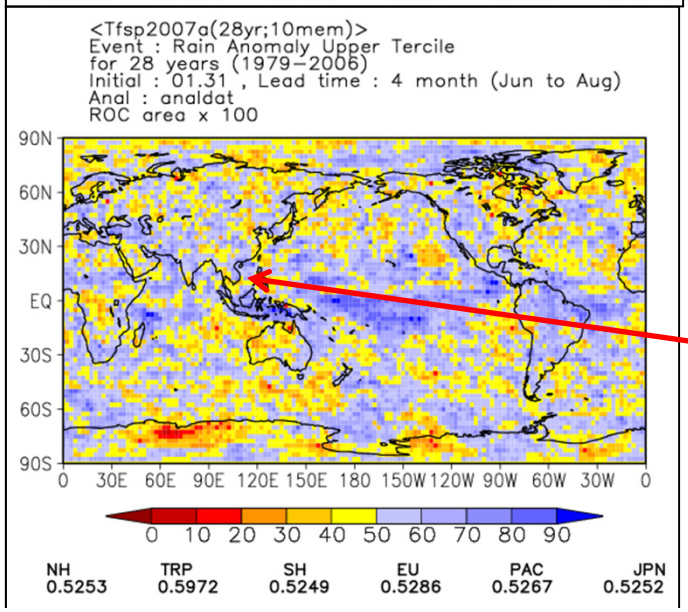

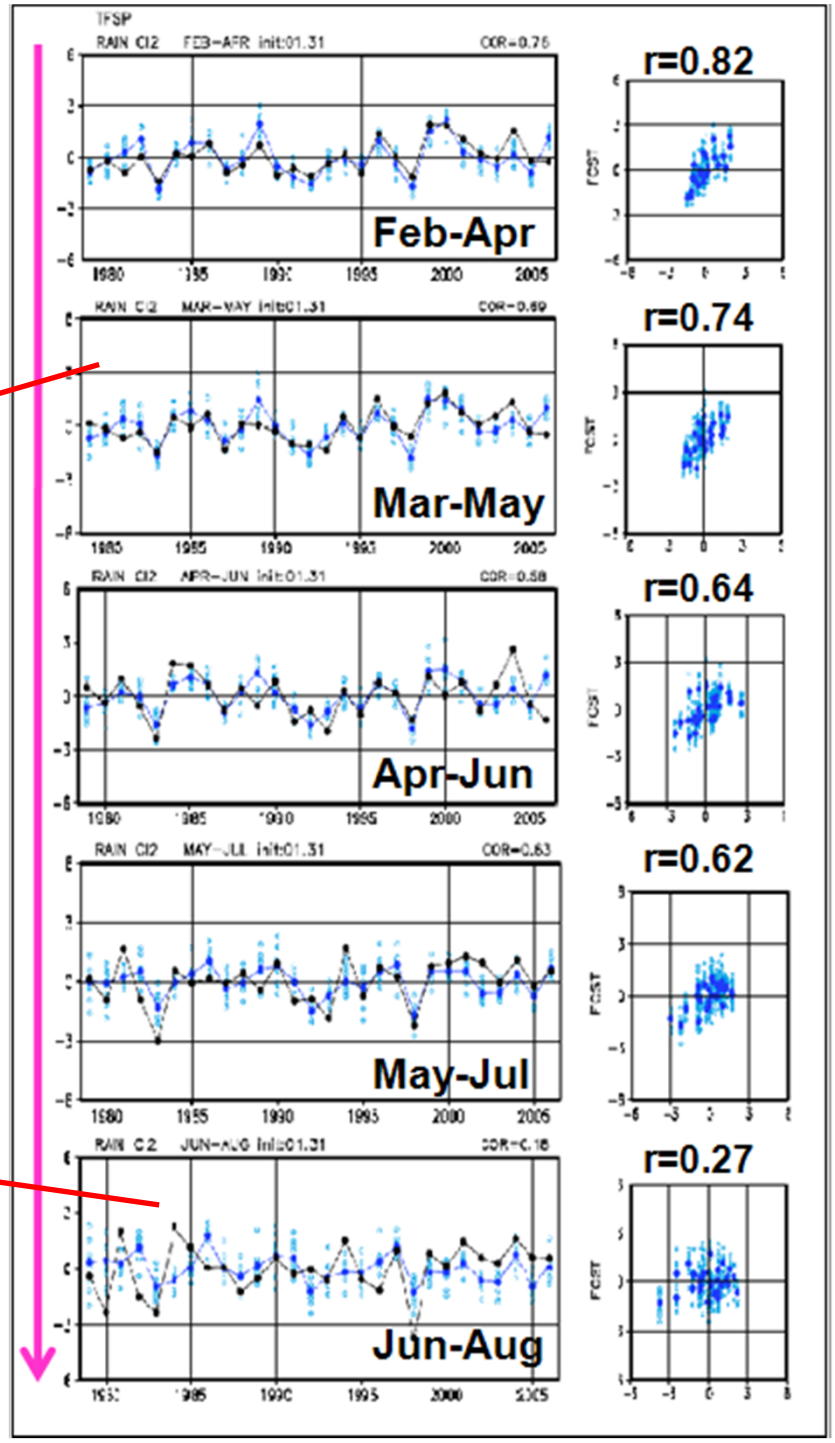

Surface air temperature over land predictions over Japan

ROC skill scores for upper tercile of surface air temperature over land prediction in Jun-Aug from the initials of Jan 31.

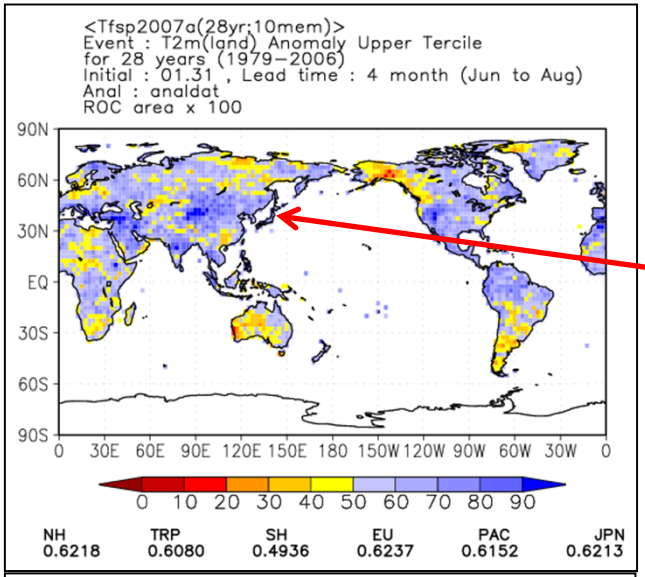

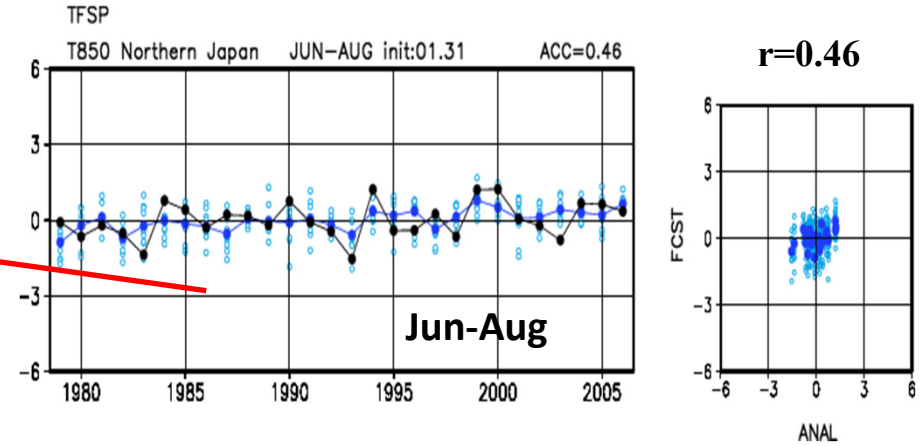

ROC skill scores for upper tercile of surface air temperature over land prediction in Dec-Feb from the initials of Oct 31.

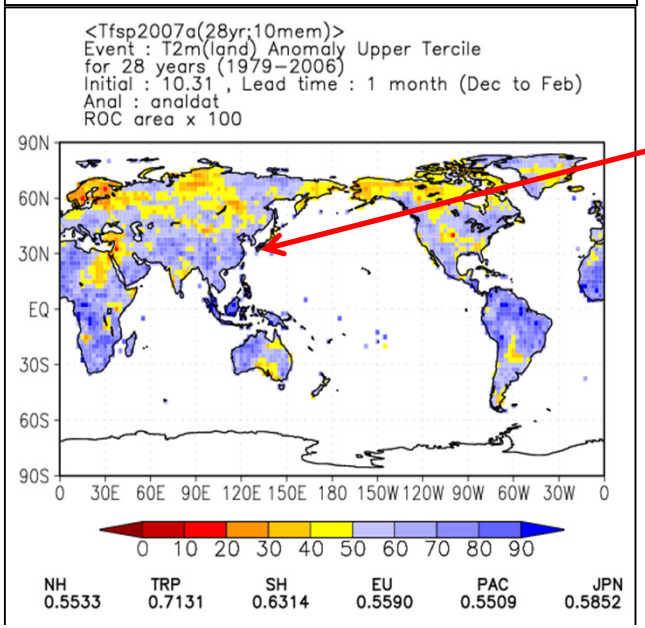

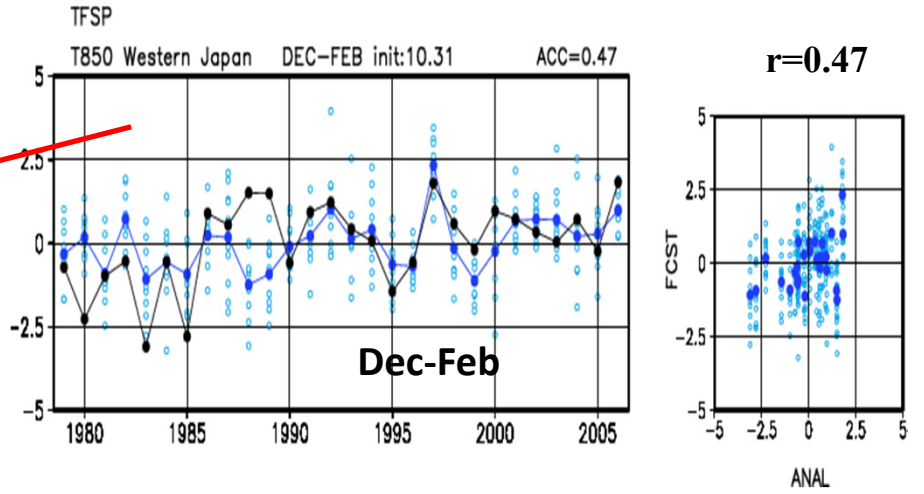

Decadal Climate Variability

G4: African Climate Variability

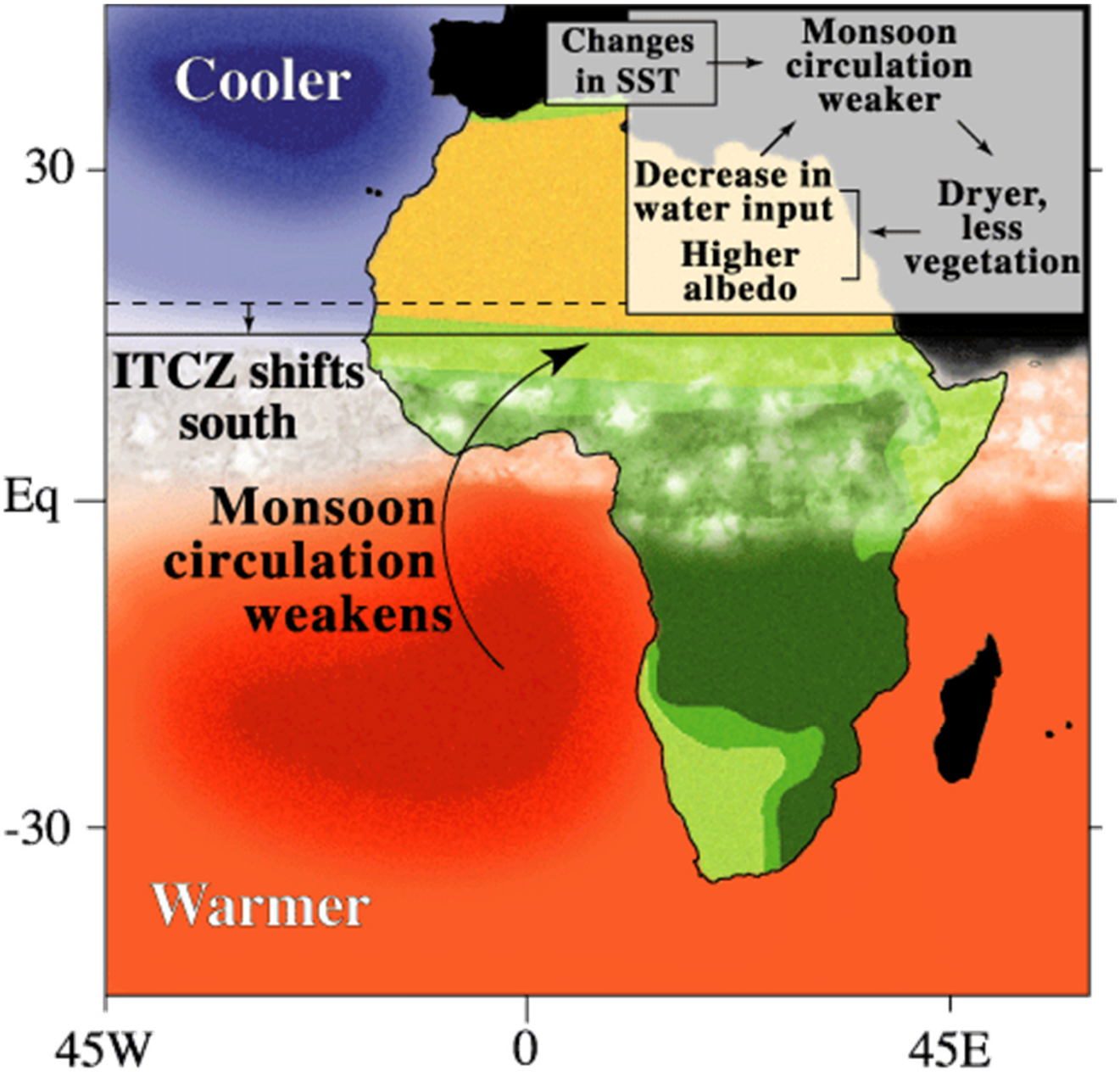

SST – Rainfall – Vegetation feedback over the Sahel region

CLIVAR AV/G4/0102

GCM Simulation of the Sahelian Rainfall

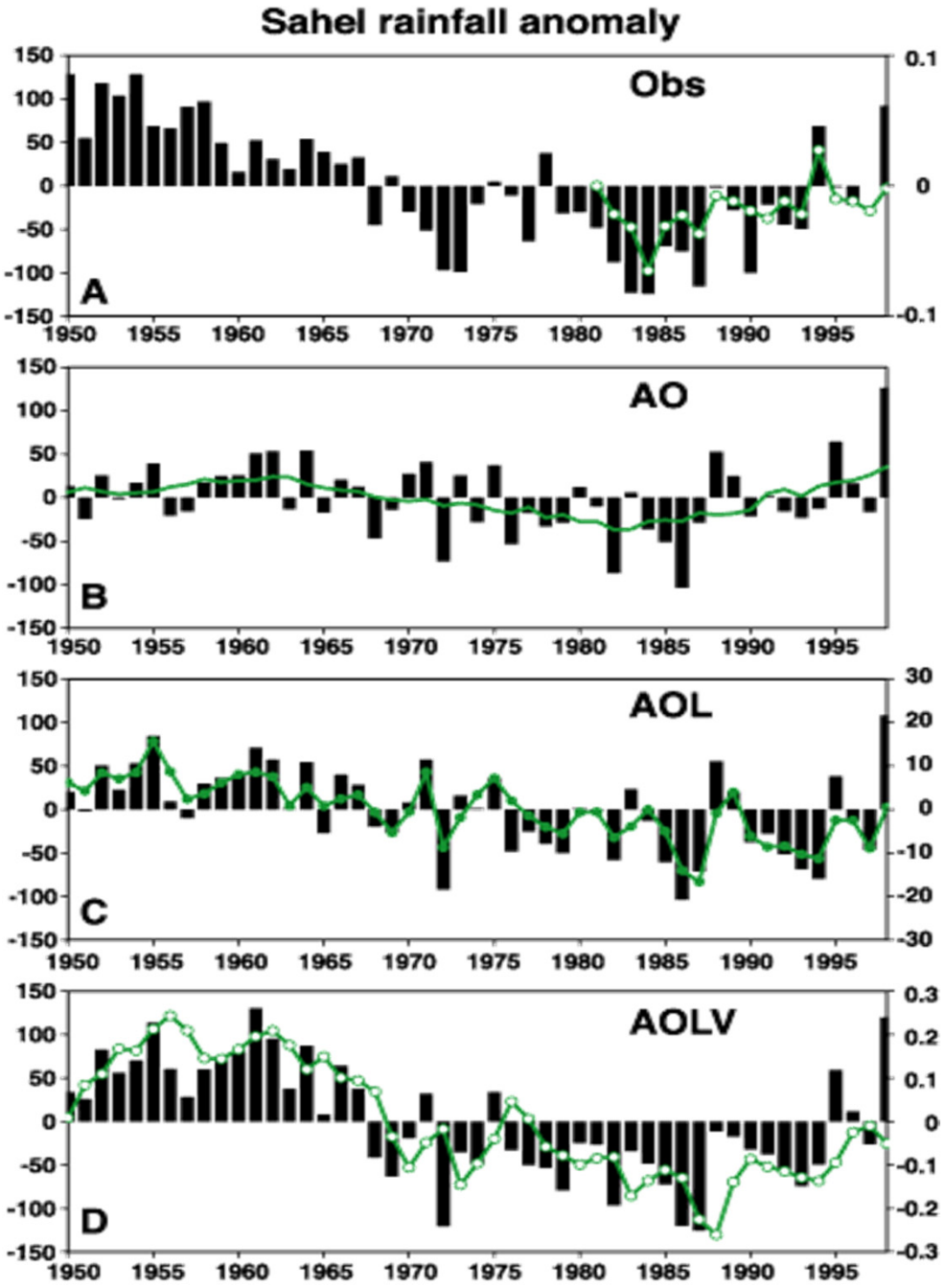

The dramatic drying trend in the Sahel from the 1950s to the 1980s is initially forced by SST (b) but amplified by soil moisture (c) and vegetation (d).

Zeng et al. (1999)

D4: Pacific and Indian Ocean Decadal Variability

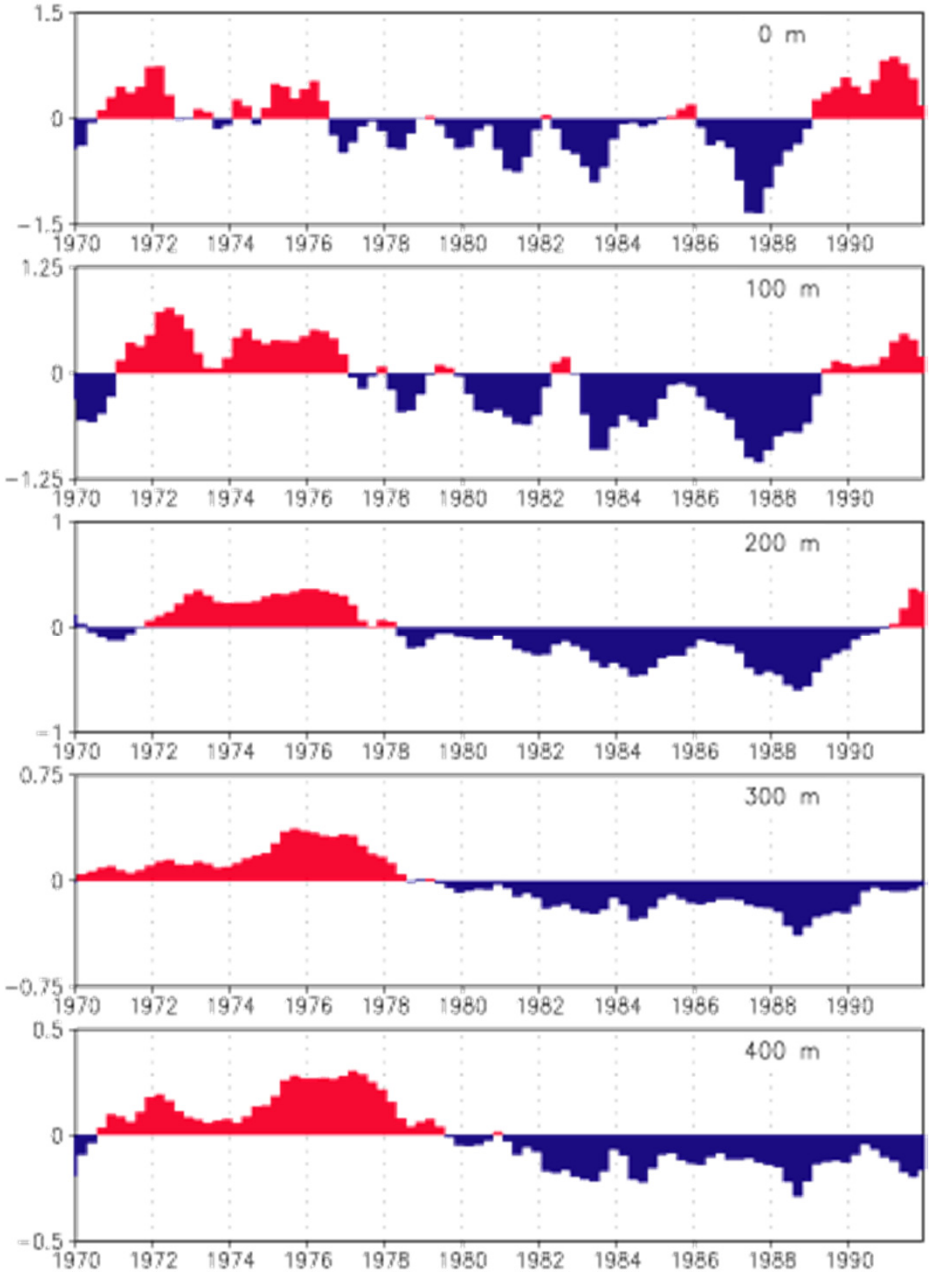

Seasonal temperature anomalies in the central North Pacific region at selected depths from 1970 to 1992 (Deser et al., 1996, JC).

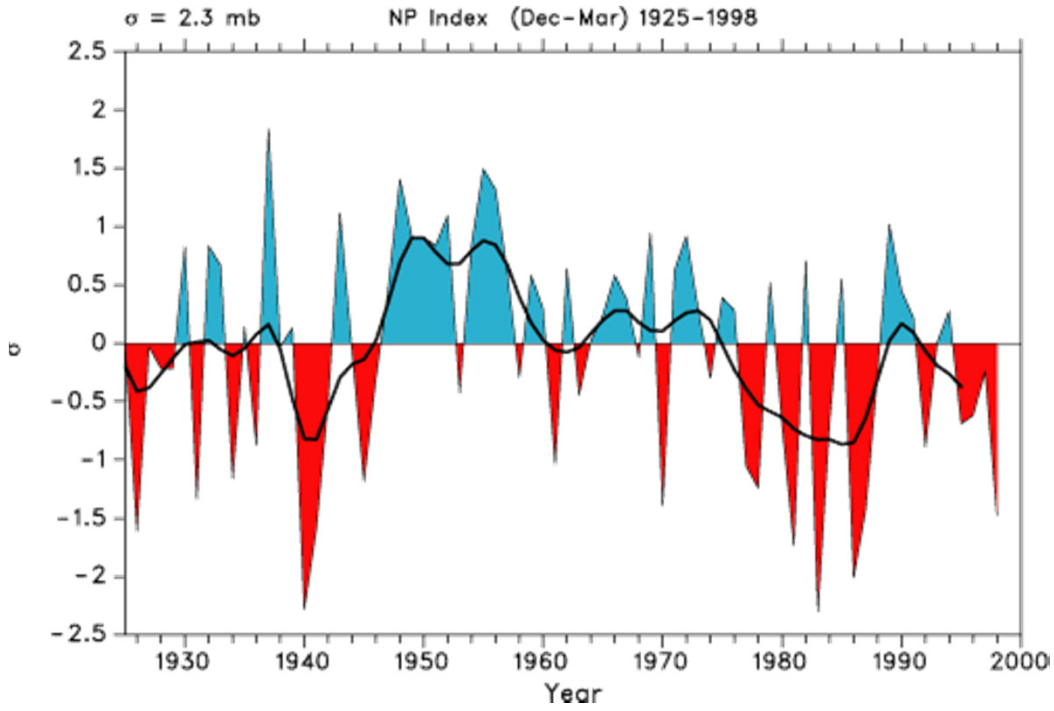

Area-averaged SLP over the region 30N-50N, 160E-140W shows a decadal time scale variability (Trenberth and Hurrell, 1994, CD).

Possible Mechanisms of the North Pacific Decadal Variability

Decadal Variability in the North Pacific

- The Subduction Hypothesis -

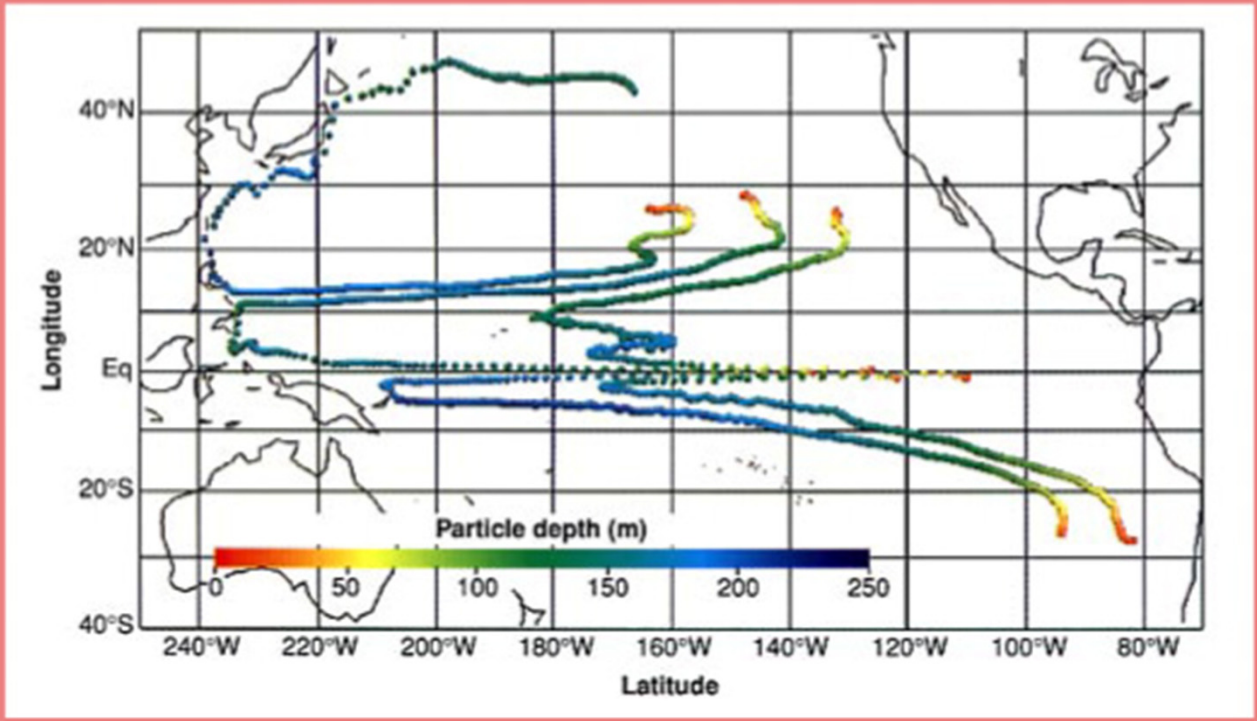

The paths of water parcels over a period of 16 years after subduction off the coasts of California and Peru as simulated by means of a realistic oceanic general circulation model forced with the observed climatological winds. From the colours, which indicate the depth of the parcels, it is evident that parcels move downward, westward, and equatorward unless they start too far to the west off California, in which case they join the Kuroshio Current. Along the equator they rise to the surface while being carried eastward by the swift Equatorial Undercurrent (Gu, Philander, 1997, Science, 275, 805-807).

AV/D4/99-2

Decadal Variability in the North Pacific

- Possible Mechanisms -

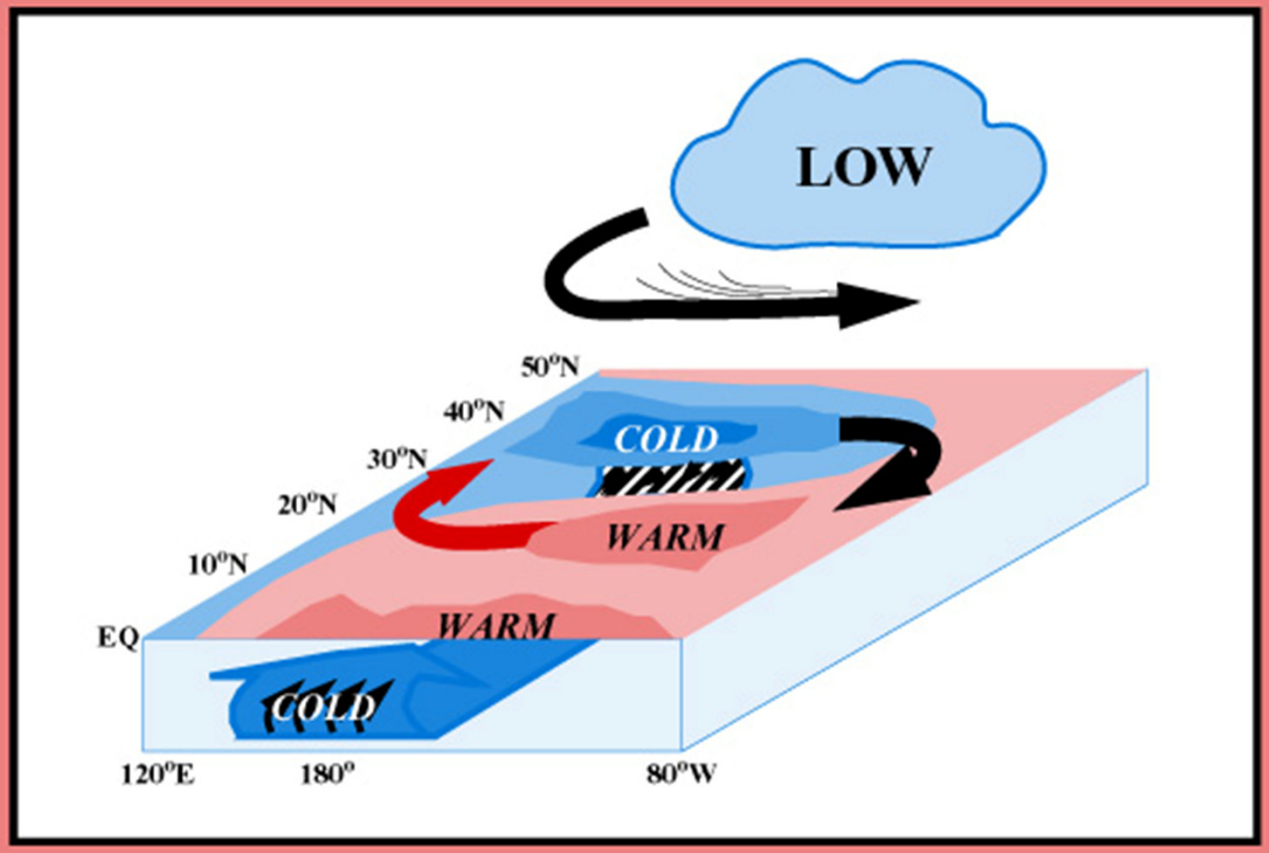

Schematic diagram of possible mechanisms of decadal climate variability. Extratropical decadal climate variability may be caused by a cycle involving unstable air-sea interactions between the subtropical gyre circulation in the North Pacific and the Aleutian low-pressure system. Long-term fluctuations of the tropical SSTs may, presumably, be induced by an influx of water from higher latitudes which subducts in the North Pacific and flows southeastward along the surfaces of constant density before equatorial upwelling brings it back to the surface. The tropical SST anomalies may in turn also affect the Aleutian low-pressure system (S. Venzke, 1998, Ocean-atmosphere interactions of decadal timescales, Thesis, Max-Planck-Institut für Meteorologie, Hamburg, 100pp).

AV/D4/99-3

D3: The Atlantic Thermohaline Circulation

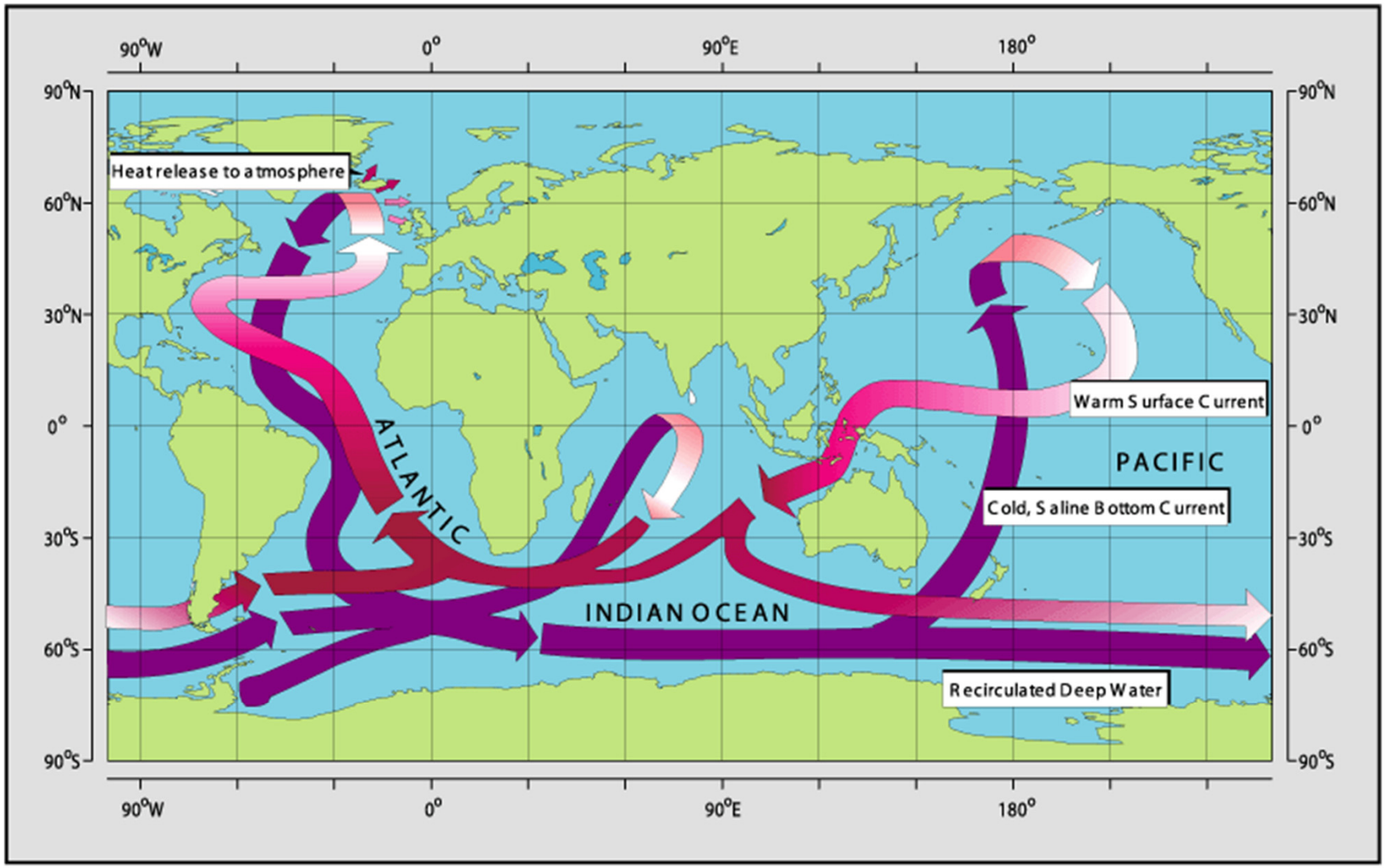

Schematic diagram of the global ocean circulation pathways, the 'conveyer' belt (after W. Broecker, modified by E. Maier-Reimer).

CLIVAR AV/D3/99-2

SAT Change after a collapse of the THC

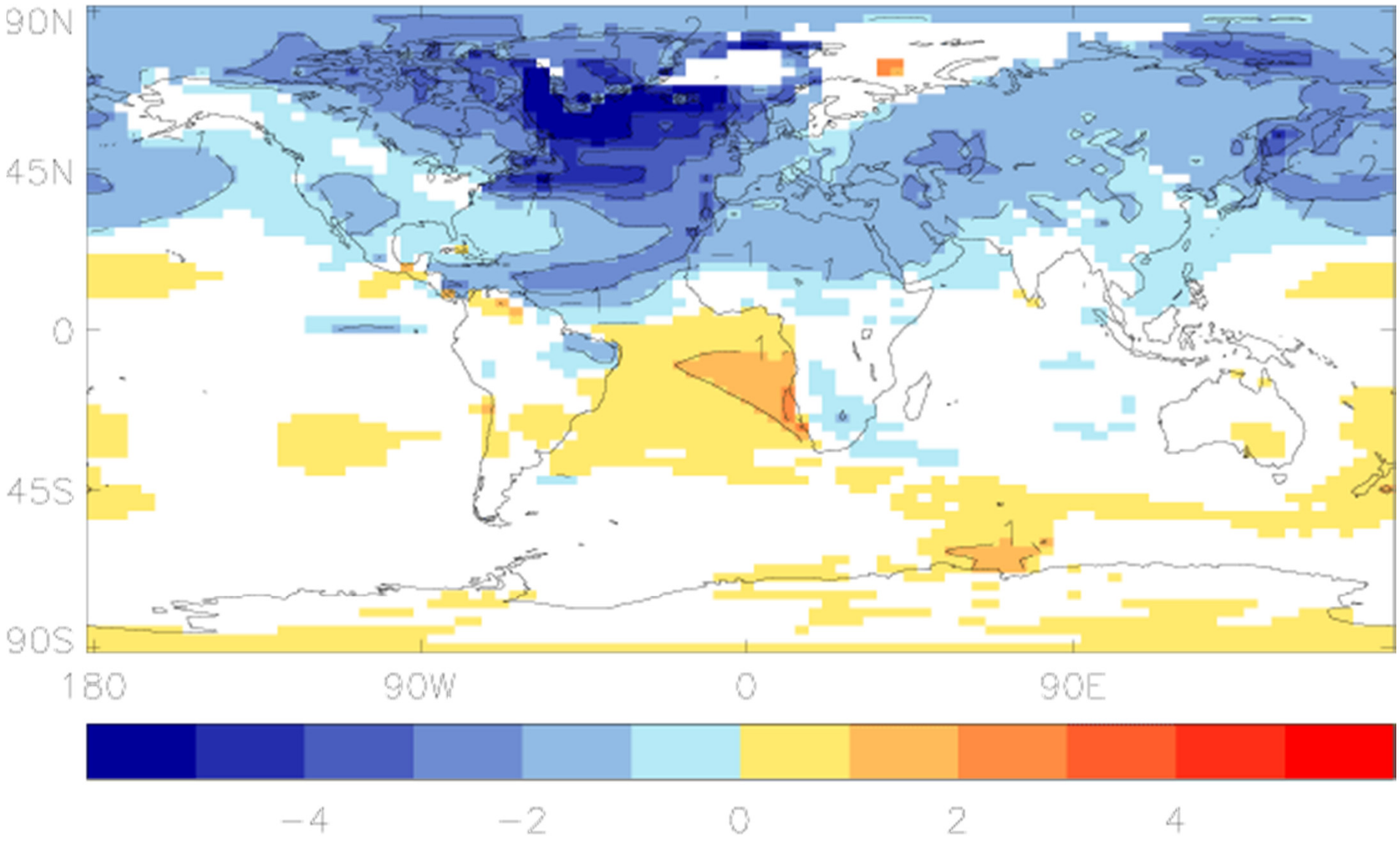

Annual mean surface air temperature change over the years 50-100 after a collapse of the THC in HadCM3.

Vellinga et al., 2002 CC

From http://www.ipcc.ch

Atlantic Thermohaline Circulation Changes

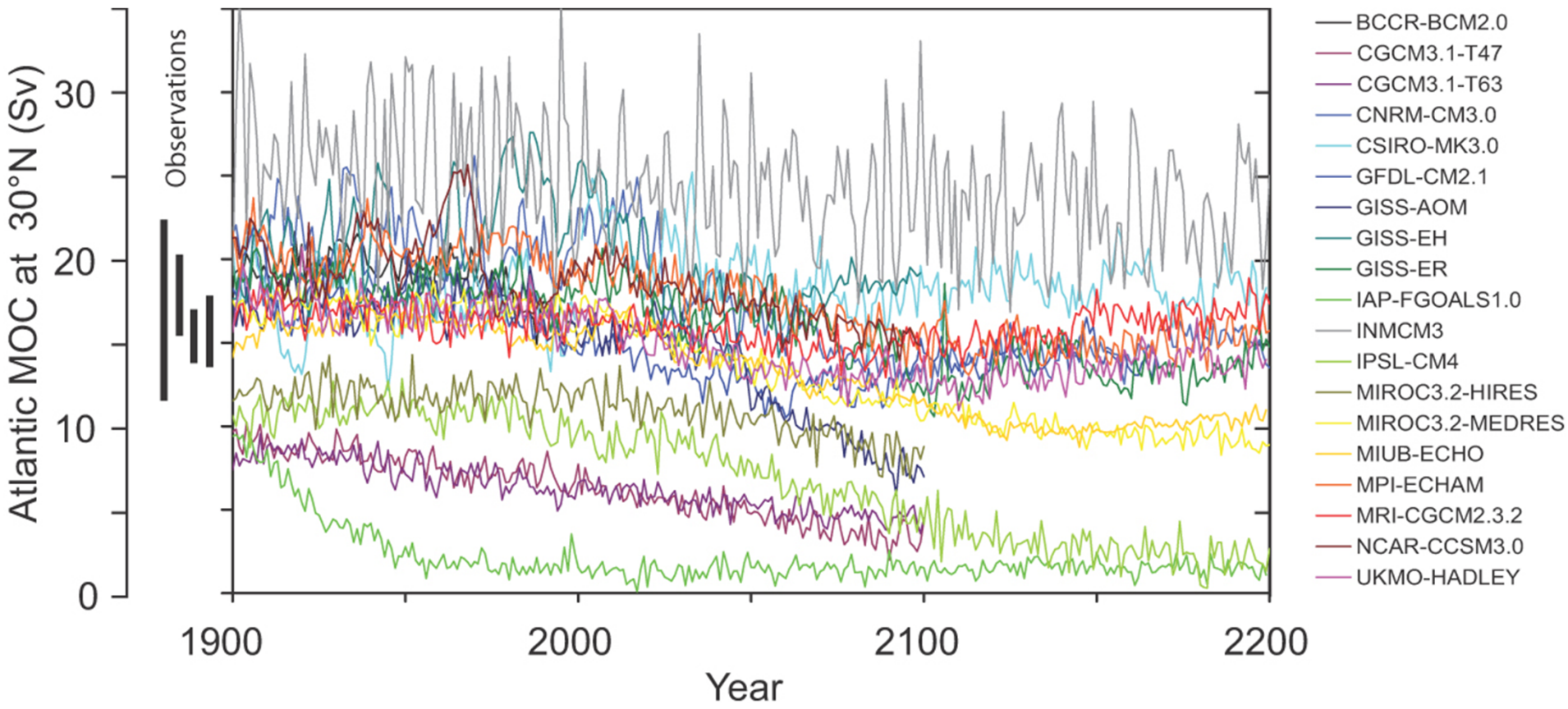

Figure 10.15. ***Evolution of the Atlantic meridional overturning circulation (MOC) at 30° N in simulations with the suite of comprehensive coupled climate models (see Table 8.1 for model details) from 1850 to 2100 using 20th Century Climate in Coupled Models (20C3M) simulations for 1850 to 1999 and the SRES A1B emissions scenario for 1999 to 2100. Some of the models continue the integration to year 2200 with the forcing held constant at the values of year 2100. Observationally based estimates of late-20th century MOC are shown as vertical bars on the left. Three simulations show a steady or rapid slow down of the MOC that is unrelated to the forcing; a few others have late-20th century simulated values that are inconsistent with observational estimates. Of the model simulations consistent with the late-20th century observational estimates, no simulation shows an increase in the MOC during the 21st century; reductions range from indistinguishable within the simulated natural variability to over 50% relative to the 1960 to 1990 mean; and none of the models projects an abrupt transition to an off state of the MOC. Adapted from Schmittner et al. (2005) with additions.***

Climate Change Prediction

From http://www.ipcc.ch

AR4 Global Mean Temperature Simulation

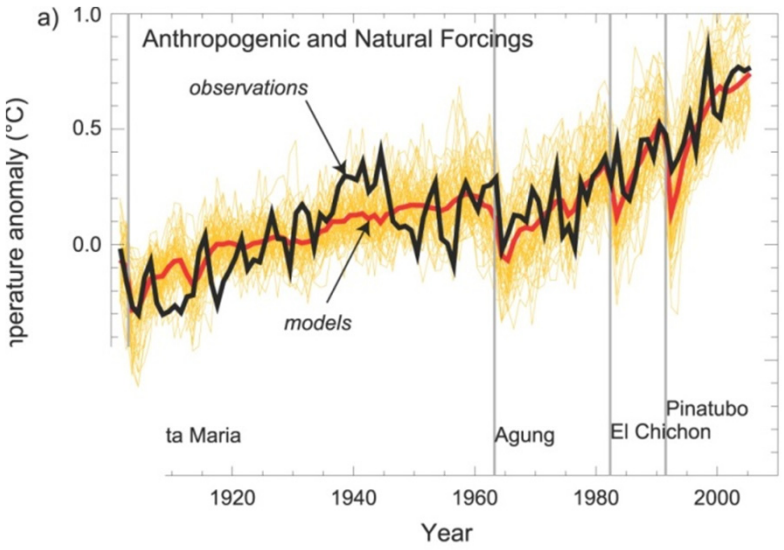

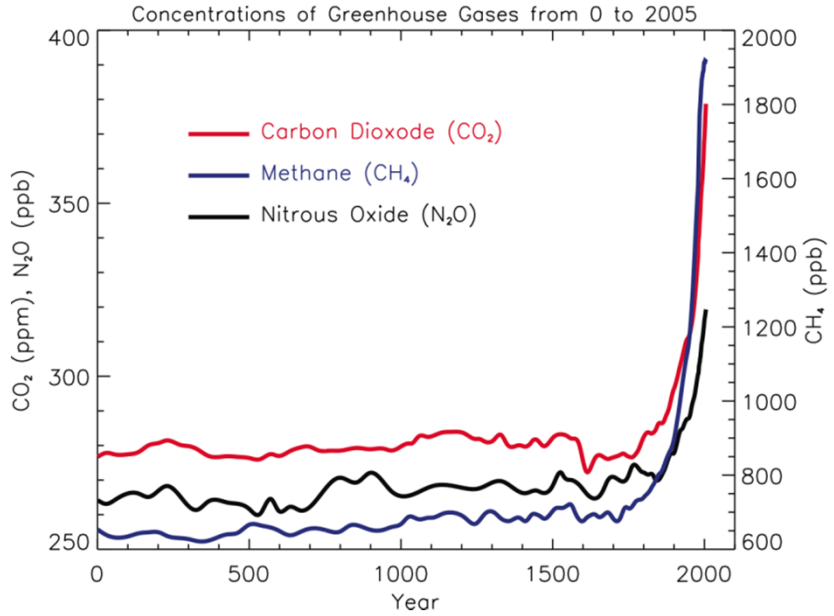

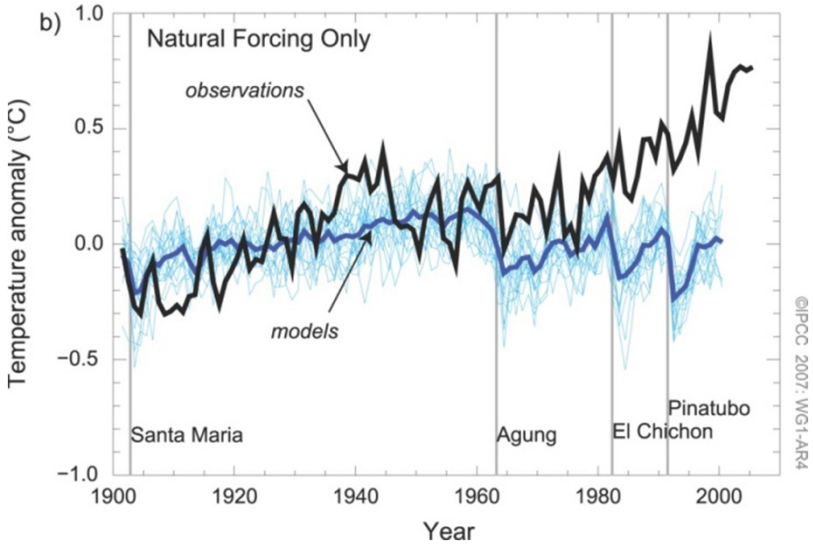

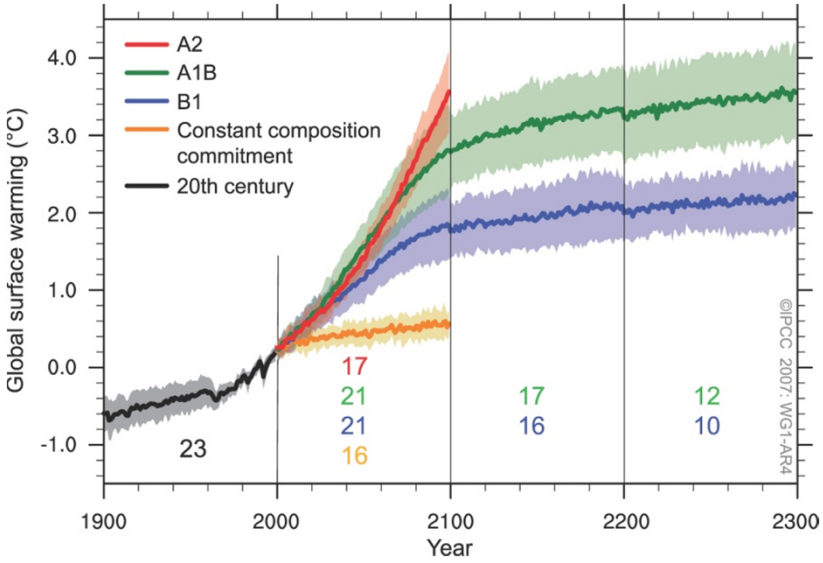

Projected Change of DJF and JJA Precipitation

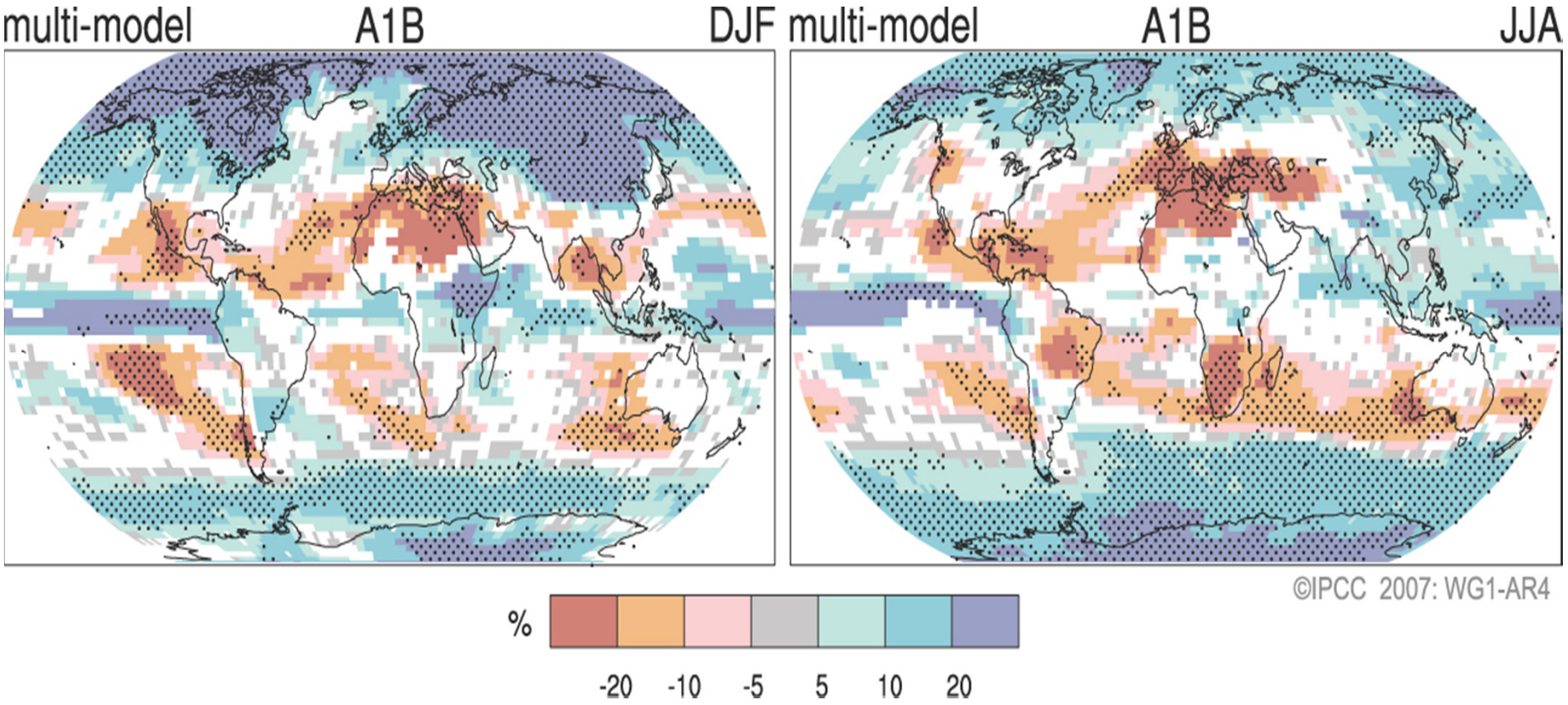

Figure SPM.7. ***Relative changes in precipitation (in percent) for the period 2090–2099, relative to 1980–1999. Values are multi-model averages based on the SRES A1B scenario for December to February (left) and June to August (right). White areas are where less than 66% of the models agree in the sign of the change and stippled areas are where more than 90% of the models agree in the sign of the change. {Figure 10.9}***

From http://www.ipcc.ch

Precipitation Intensity and Dry days

From http://www.ipcc.ch

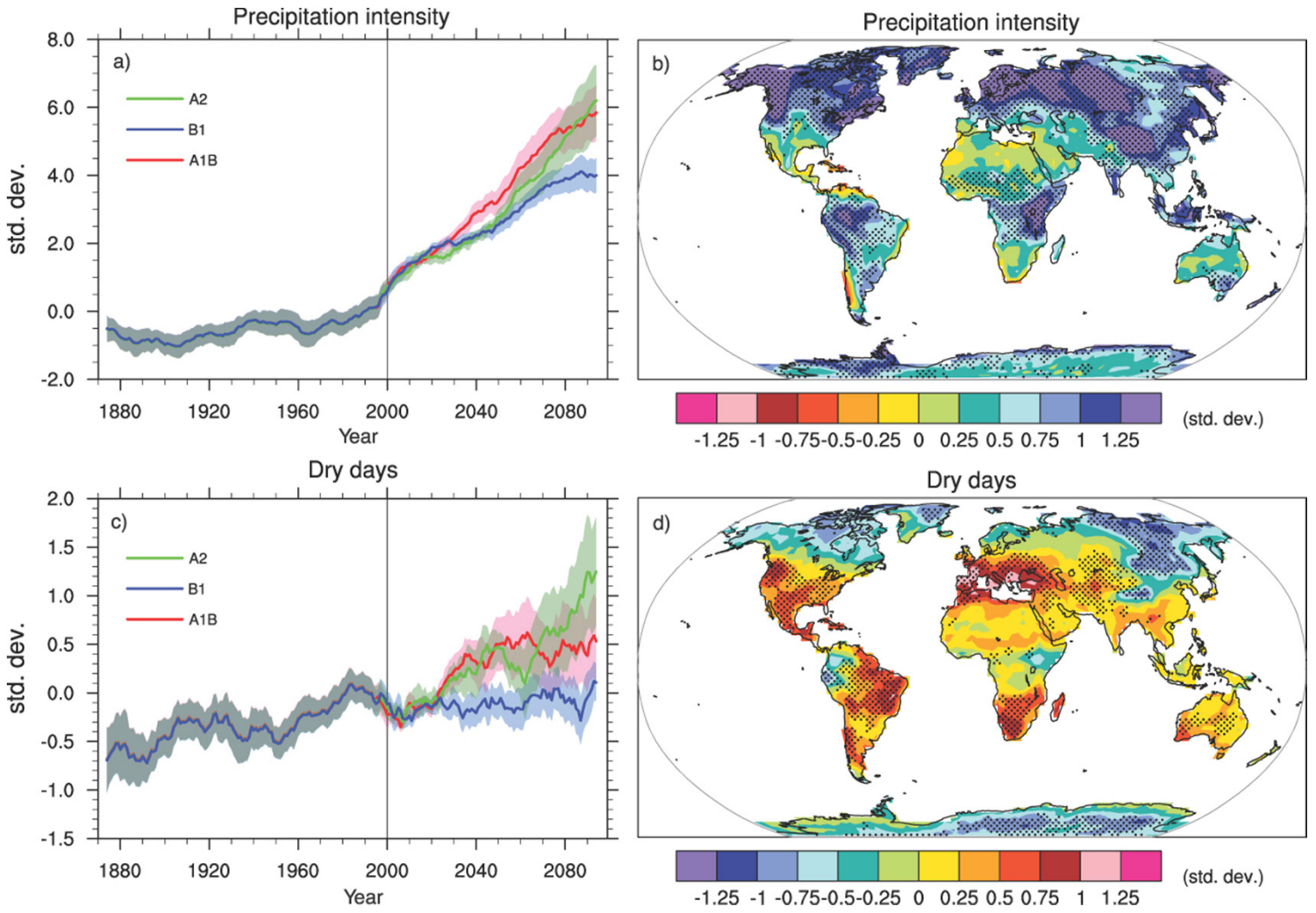

Figure 10.18. ***Changes in extremes based on multi-model simulations from nine global coupled climate models, adapted from Tebaldi et al. (2006). (a) Globally averaged changes in precipitation intensity (defined as the annual total precipitation divided by the number of wet days) for a low (SRES B1), middle (SRES A1B) and high (SRES A2) scenario. (b) Changes in spatial patterns of simulated precipitation intensity between two 20-year means (2080–2099 minus 1980–1999) for the A1B scenario. (c) Globally averaged changes in dry days (defined as the annual maximum number of consecutive dry days). (d) Changes in spatial patterns of simulated dry days between two 20-year means (2080–2099 minus 1980–1999) for the A1B scenario. Solid lines in (a) and (c) are the 10-year smoothed multi-model ensemble means; the envelope indicates the ensemble mean standard deviation. Stippling in (b) and (d) denotes areas where at least five of the nine models concur in determining that the change is statistically significant. Extreme indices are calculated only over land following Frich et al. (2002). Each model's time series was centred on its 1980 to 1999 average and normalised (rescaled) by its standard deviation computed (after de-trending) over the period 1960 to 2099. The models were then aggregated into an ensemble average, both at the global and at the grid-box level. Thus, changes are given in units of standard deviations.***

From http://www.ipcc.ch

Sea Level Change

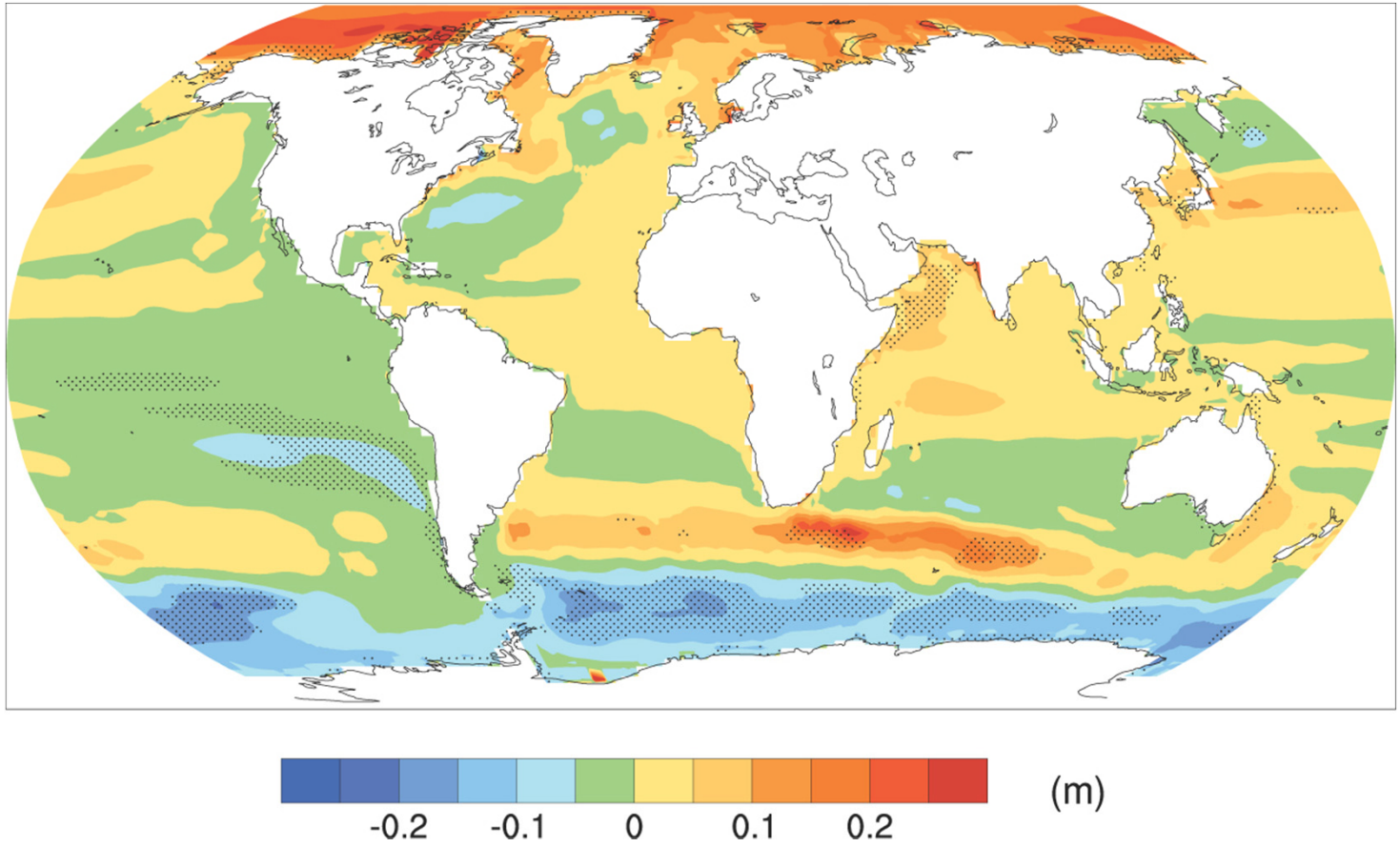

Figure 10.32. ***Local sea level change (m) due to ocean density and circulation change relative to the global average (i.e., positive values indicate greater local sea level change than global) during the 21st century, calculated as the difference between averages for 2080 to 2099 and 1980 to 1999, as an ensemble mean over 16 AOGCMs forced with the SRES A1B scenario. Stippling denotes regions where the magnitude of the multi-model ensemble mean divided by the multi-model standard deviation exceeds 1.0.***

http://www.jamstec.go.jp/kakushin21/eng/brochure/general%20report-e.pdf

Innovative Program of Climate Change Projection for the 21st Century

Future Change in Tropical Cyclones

Projection of the Change in Future Weather Extremes Using Super-High-Resolution Atmospheric Models

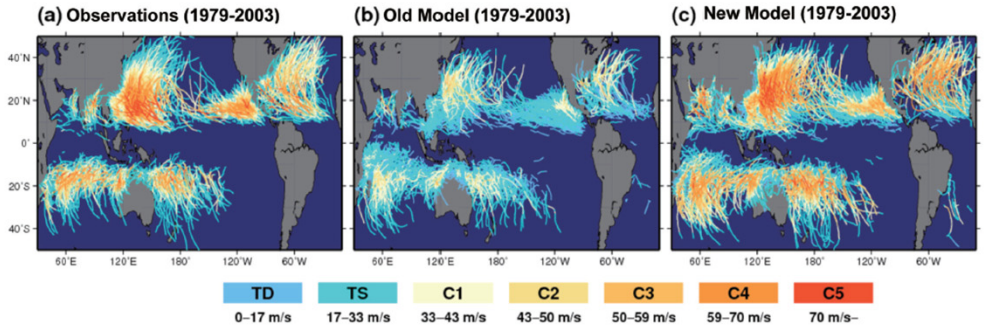

Figure 1. Global distribution of tropical cyclones for (a) observations, (b) the present-day simulation using the old model, and (c) using the new model. Tropical cyclone tracks

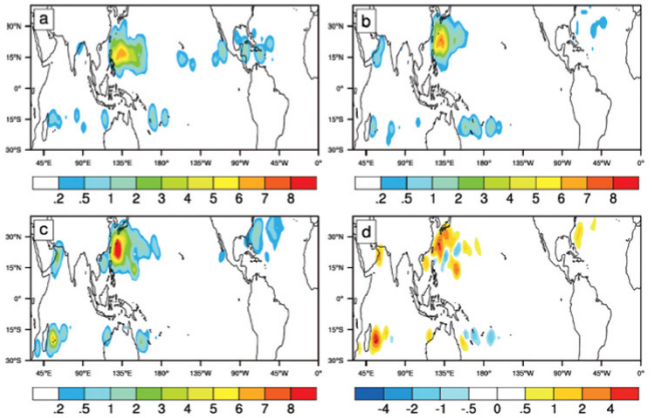

Figure 2. Tropical cyclone frequency of Category 5 storms for (a) observations (1979—2003), (b) present-day simulation by the new model (1979—2003), (c) future simulation, and (d) future changes. Unit is number per 25 years.

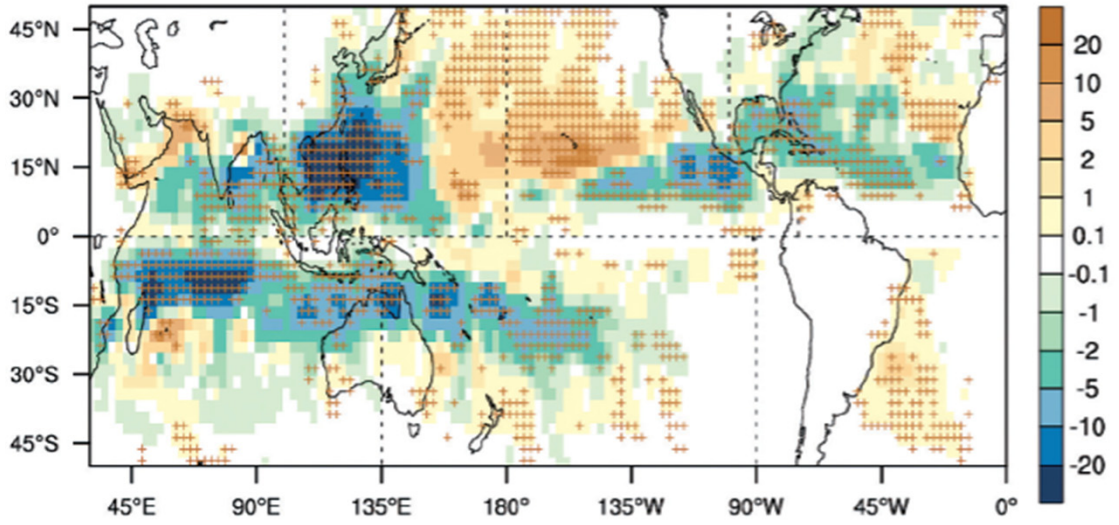

Figure 3. Ensemble mean future changes in tropical cyclone frequency. Unit is number per 25 years. Cross marks indicate that more than 10 experiments out of 12 experiments project the same sign.

SUMMARY

- Unusual weather and climate are attributed to unusual atmospheric flows, storms and convective disturbance. Diagnostic analysis shows that those disturbances are often related to atmospheric intrinsic waves and phenomena.
- However, atmospheric environment is maintained by other elements sustaining the climate system. Sometimes, unusual and steady convective activity is connected to long-term SST anomalies related to ocean variability.

- Radiative processes including longwave absorption by greenhouse gases and shortwave reflection by snow, ice, clouds and aerosols determine the local Earth's ground temperature.
- The distribution of ground temperature is influential to vertical and horizontal atmospheric and oceanic stabilities, the amount of water vapor and the speed of water cycle. Then, those can affect atmospheric and oceanic flows, the features of storms and convections and eventually our daily lives.
- Therefore, we need to continue careful watches and diagnostics for global and local climate systems, as well as its future projection.